



The effect of La³⁺-doping of CeO₂ support on the water-gas shift reaction mechanism and kinetics over Pt/Ce_{1-x}La_xO_{2-δ}

Christos M. Kalamaras, Klito C. Petallidou, Angelos M. Efstathiou*

Department of Chemistry, Heterogeneous Catalysis Laboratory, University of Cyprus, University Campus, P.O. Box 20537, CY 1678 Nicosia, Cyprus

ARTICLE INFO

Article history:

Received 2 October 2012
Received in revised form 14 January 2013
Accepted 2 February 2013
Available online 13 February 2013

Keywords:

WGS reaction mechanism
La³⁺-doping
Ceria-supported Pt
SSITKA-DRIFTS
SSITKA-MS
Operando studies

ABSTRACT

Platinum nanoparticles ($d_{\text{Pt}} = 1.0\text{--}1.2\text{ nm}$) supported on single CeO₂ and La₂O₃ metal oxides and Ce_{0.8}La_{0.2}O_{2-δ} solid solution were prepared to investigate for the first time the effect of La³⁺-doping of ceria on important mechanistic and kinetic aspects of the water-gas shift (WGS) reaction, namely: (i) the concentration and chemical structure of *active* adsorbed reaction intermediates present in the C-path and H-path of WGS at 250 and 300 °C, (ii) the chemical nature of *inactive* species formed during WGS, and (iii) the prevailing mechanistic path among “redox” and “associative” both proposed in the literature. For this, steady-state isotopic transient kinetic analysis (SSITKA) experiments coupled with in situ DRIFTS and mass spectrometry were performed to follow the H-path (use of D₂O) and C-path (use of ¹³CO) of the WGS. In addition, other transient isotopic experiments using *operando* methodology (use of DRIFTS and mass spectrometry) were designed to follow with time on stream the reactivity toward water of the various adsorbed species formed under WGS. It is proposed that on Pt/Ce_{1-x}La_xO_{2-δ} ($x = 0.0, 0.2$ and 1.0) the WGS reaction follows both the “redox” and “associative” mechanisms but the extent of participation of each mechanism to the overall WGS reaction rate depends on the support chemical composition. The WGS kinetic rate ($\mu\text{mol CO g}^{-1} \text{s}^{-1}$) increased by a factor of 2.0 and 2.8 at 300 °C on 0.5 wt% Pt supported on Ce_{0.8}La_{0.2}O_{2-δ} compared to CeO₂ and La₂O₃, respectively. This was explained by (i) the larger concentration of *active* surface intermediates formed around each Pt nanoparticle (larger extent of reactive zone) and (ii) the higher reactivity of sites (k, s^{-1}) responsible for CO₂ and H₂ formation on Pt/Ce_{0.8}La_{0.2}O_{2-δ} compared to Pt/CeO₂ and Pt/La₂O₃. Active –OH groups is suggested to be formed on defect sites (Ce³⁺–□_o) of Ce_{0.8}La_{0.2}O_{2-δ} as a consequence of the introduction of La³⁺ into the ceria lattice, the latter enhancing the concentration of labile oxygen and its surface mobility, important characteristics of the “redox” mechanism.

© 2013 Elsevier B.V. All rights reserved.

1. Introduction

The development of a strategy for power production based on hydrogen gas (hydrogen being the energy carrier) with significant advantages has recently attracted considerable attention [1,2]. Toward this goal, there is an important need to produce H₂(g) in an efficient and environmentally acceptable way and with minimum cost [3]. The concomitant development of a fuel processor in which carbonaceous fuels are converted into hydrogen gas is also receiving an increasing attention [4]. The heterogeneously catalyzed water-gas shift (WGS) reaction ($\text{CO} + \text{H}_2\text{O} \rightleftharpoons \text{CO}_2 + \text{H}_2$, $\Delta H^\circ = -41.2\text{ kJ/mol}$) is one of the *key steps* in a fuel processing system for H₂ production, including steam reforming of hydrocarbons, sugars, alcohols and bio-oil. This chemical step increases

H₂(g) concentration and at the same time decreases the CO(g) concentration in the produced H₂-rich gas stream [5–9].

Platinum supported on reducible metal oxide carriers appear to be promising catalytic systems for low-temperature WGS compared to conventionally used WGS catalysts [10]. To increase the catalytic activity of supported Pt solids, various supports including: CeO₂ [8,11–18], TiO₂ [19–21], La₂O₃ [22–24] and ZrO₂ [13–15,25,26] (single or mixed) have been examined. However, the stability of these catalytic systems under practical WGS reaction conditions still needs to be improved [27]. The fundamental understanding of the WGS reaction at the molecular level is of paramount importance in order to design proper functional catalytic materials for activity, selectivity and stability optimization under industrial WGS reaction conditions. To achieve this goal, it is necessary to investigate mechanistic aspects of the WGS reaction by performing in a correct manner in situ spectroscopic and kinetic studies under reaction conditions (*operando* studies) [28,29].

It is generally accepted that the WGS reaction over metal oxide-supported noble metal catalysts operates in a bifunctional

* Corresponding author. Tel.: +357 22 892776; fax: +357 22 892801.
E-mail address: efstath@ucy.ac.cy (A.M. Efstathiou).

manner with the participation of both the dispersed metal phase and the support. In this regard, two general mechanistic schemes have been proposed: (i) the “redox or regenerative” mechanism [19,30–35], according to which CO adsorbed on the metal phase is oxidized toward CO₂ by labile oxygen of support, the latter being re-oxidized by water leading to the formation of hydrogen, and (ii) the “adsorptive or associative” mechanism [16–19,36–40] according to which the reaction proceeds via the interaction of adsorbed CO with terminal hydroxyl groups of the oxidic support to form “carbon-containing” intermediates, namely: formate, carboxyl, carbonate or bicarbonate, which further react or decompose to form CO₂ and H₂. Recently, Gokhale et al. [41] and Grabow et al. [42] have demonstrated via microkinetic model, DFT computations and experimental data that carboxyl (COOH) is the main reactive intermediate for the low-*T* (250–300 °C) WGS reaction on Pt(1 1 1) and Cu(1 1 1) surfaces, whereas formate (HCOO) acts only as a spectator species. Thermodynamic and kinetic parameters for the microkinetic model were derived from periodic, self-consistent density functional theory (DFT-GGA) calculations related to the Pt(1 1 1) surface.

Several important kinetic and mechanistic aspects of the WGS at 1 atm still remain controversial issues over supported metal catalysts, namely: the dominant mechanistic path, the rate-determining step, the chemical nature of the *active* “carbon-containing” and “hydrogen-containing” intermediates, and their true site location (e.g., support, metal–support interface, metal surface or metal and support surfaces) [16,28,43–47].

In the present work, the WGS reaction in the 250–300 °C range has been investigated over Pt nanoparticles (1.0–1.2 nm) supported on CeO₂, Ce_{1–x}La_xO_{2–δ} and La₂O₃ with the goal to understand the effect of La³⁺-doping of ceria on important kinetic and mechanistic aspects of the reaction at hand. Toward this goal, steady-state isotopic transient kinetic analysis (SSITKA) and other transient isotopic experiments coupled with DRIFTS and mass spectrometry have been designed and performed in order to: (a) gather information on the chemical structure of *active* reaction intermediates and *spectator* species, (b) estimate the surface concentration of *active* “H-containing” and “C-containing” intermediates found in the H-path and C-path of the WGS reaction, respectively, and (c) reveal the prevailing mechanism among “redox” and “associative” when Pt nanoparticles of similar size are supported on CeO₂, Ce_{1–x}La_xO_{2–δ} and La₂O₃ carriers.

2. Experimental

2.1. Catalyst preparation and characterization

The Ce_{1–x}La_xO_{2–δ} mixed metal oxide and the single metal oxides of CeO₂ and La₂O₃ used as supports of platinum were synthesized using a modified citrate sol–gel technique. In particular, appropriate amounts of Ce(NO₃)₃·6H₂O and La(NO₃)₃·6H₂O (e.g., based on Ce_{0.8}La_{0.2}O₂ composition) were dissolved in distilled water. The solution pH was kept at 2.0 by dropwise addition of nitric acid solution (5 M). Then, citric acid of 1.5 times the total molar amount of metal ions (*M*_{tot}) in solution was added. The resulting solution was subsequently heated to 70 °C under stirring for assisting polymerization/condensation reactions. Finally, a gel-like yellowish material was obtained. After drying at 110 °C for 17 h, the gel became spongy. A heating step in air was subsequently applied, where self-ignition took place at 350 °C. The material was further kept at 400 °C for 30 min. After grinding, the resulting material was placed in an oven at 600 °C for 10 h to eliminate all the organic residues remained after the synthesis procedure. More details on the procedure followed are described elsewhere [48]. The supported-Pt catalysts were prepared by impregnating the oxidic supports with

a given amount of diluted aqueous solution of H₂PtCl₆ (8 wt% solution in water, Aldrich) so as to yield a 0.5 wt% Pt nominal loading. After gradual evaporation of water in the slurry at 70 °C for 4 h, the resulting solid was dried at 120 °C overnight and then placed in a furnace (ELF 11/6, carbolite) for calcination at 600 °C in static air for 2 h (heating rate of 30 °C min^{–1} from 25 to 600 °C). Prior to catalytic measurements, the fresh catalyst sample was in situ pre-treated in 20 vol% O₂/He (50 N mL min^{–1}) gas mixture at 600 °C for 2 h followed by reduction in H₂ (1 bar, 50 N mL min^{–1}) at 300 °C for 2 h.

The specific surface area (m² g^{–1}) of the solids was estimated by applying the BET method. N₂ adsorption–desorption isotherms obtained at 77 K over the entire range of relative pressures on samples previously outgassed at 300 °C for 2 h (Micromeritics Gemini III apparatus) were used to estimate the mean pore size, *d_p* (nm) of the porous solids. Platinum particle size distribution and a mean Pt particle size (*d_{pt}*, nm) was directly measured by high angle annular dark field (HAADF) images obtained using a 200 kV JEM-2100J (Jeol Ltd.) transmission electron microscope equipped with an INCA-Sight (Oxford Inc.) energy-dispersive X-ray spectroscopy for the 0.5 wt% Pt/CeO₂, 0.5 wt% Pt/Ce_{0.8}La_{0.2}O_{2–δ}, and 0.5 wt% Pt/La₂O₃ catalysts. HAADF images were recorded with the microscope in the STEM mode with a beam size of 1 nm and an inner collection angle of 68.5 mrad. The contrast in HAADF images is mainly due to differences in the atomic number (*Z*) of metal elements at constant thickness. Given that *Z*_{Pt} = 78, *Z*_{Ce} = 58, and *Z*_{La} = 57, the brighter regions in the HAADF images correspond to Pt nano-particles. Platinum dispersion was estimated after considering the relationship: *D*(%) = 1.1/*d_{pt}* (nm) × 100.

2.2. Steady-state WGS reaction performance

Steady-state WGS catalytic measurements were conducted in the experimental set-up previously described [49]. The reaction feed composition used consisted of 3 vol% CO/10 vol% H₂O/87 vol% He, and the total volume flow rate was 200 N mL min^{–1}, resulting in a GHSV of about 40,000 h^{–1} (L/L_{cat}/h). The powder catalyst's particle size was between 0.1 and 0.2 mm, and the amount of catalyst sample used was 0.5 g. The performance of the Pt/Ce_{1–x}La_xO_{2–δ} (*x* = 0.0, 0.2 and 1.0) catalysts in terms of *X*_{CO} (%) versus the reaction temperature was evaluated in the 200–450 °C range over a pre-reduced catalyst in H₂ flow (50 mL min^{–1}) at 300 °C for 2 h. After 1 h on reaction stream, where pseudo-steady-state reaction rate was achieved, the catalyst temperature was stepwise increased to the next temperature to be investigated. The effluent gas stream from the micro-reactor, after removing the water via a Peltier Gas Cooler (model ECP1000, M&C TechGroup), was directed to a Mass Spectrometer (Omnistar, Balzer) for the *on line* monitoring of H₂ (*m/z* = 2), CO (*m/z* = 28) and CO₂ (*m/z* = 44) gases. Calibration of the MS signals to concentrations (mol%) was performed using standard calibration gas mixtures of H₂, CO and CO₂ in diluent He gas. For the quantification of CO, the *m/z* = 28 MS signal due to cracking of CO₂ in the ionization chamber of the MS was subtracted from the overall *m/z* = 28 signal recorded (due to the presence of CO and CO₂). The purity of all gases (e.g., H₂, He, CO, Ar; Linde Gas, Greece) used in the catalytic experiments was higher than 99.95%.

2.3. SSITKA-mass spectrometry studies

The isotopes used in the SSITKA experiments were ¹³CO (99.9 at% ¹³C, Spectra Gases, Inc.) and deuterium oxide (D₂O, 99.96 at% *D*, Aldrich). SSITKA-MS experiments were performed in the apparatus described elsewhere [49], where for the addition of H₂O and D₂O in the reaction feed stream two temperature-controlled saturators with pressure monitoring system were used. The SSITKA-MS experiments performed to follow the H-path of WGS reaction involved the switch 3 vol% CO/10 vol% H₂O/Ar/Kr

(T , 30 min) \rightarrow 3 vol% $\text{CO}/10\text{ vol}\% \text{ D}_2\text{O}/\text{Ar}$ (T , t), whereas those to follow the C-path of WGS involved the switch 3 vol% $^{12}\text{CO}/10\text{ vol}\% \text{ H}_2\text{O}/\text{Ar}/\text{He}$ (T , 30 min) \rightarrow 3 vol% $^{13}\text{CO}/10\text{ vol}\% \text{ H}_2\text{O}/\text{Ar}$ (T , t). The effluent wet gas stream from the reactor was first passed through a condenser (Peltier system of low volume), the exit of which (dry gas) was directed to a mass spectrometer for *on line* recording of the normal and isotope-containing (D , ^{13}C) reactants and products (e.g., H_2 , HD, D_2 , ^{12}CO , ^{13}CO , $^{12}\text{CO}_2$ and $^{13}\text{CO}_2$) [16,17,49]. More details on the SSITKA-MS experiments and the micro-reactor used were previously reported [16,17,50–52]. Based on the transient response curve of Ar to the switch $\text{He} \rightarrow 1\text{ vol}\% \text{ Ar}/\text{He}$ [50], it was estimated that the response time (τ , s) of the system used in the SSITKA-MS studies (switching valve \rightarrow micro-reactor \rightarrow condenser \rightarrow mass spectrometer) was ~ 5 s. The mass of the catalyst was adjusted in every SSITKA-MS experiment so as to keep the CO conversion below 15%. The total mass of the catalytic bed was 0.5 g (catalyst + SiO_2 for dilution when needed).

2.4. SSITKA-DRIFTS studies

SSITKA-DRIFTS experiments were performed in a specially designed gas flow-system where the response time of the DRIFTS reactor cell (~ 80 mg $\text{Pt}/\text{Ce}_x\text{La}_{1-x}\text{O}_2$) was about 5 s at the flow rate of 200 N mL min^{-1} [51]. Signal averaging was set to 50 scans per spectrum, and the spectra were collected in the $4000\text{--}500\text{ cm}^{-1}$ range at the rate of 0.2 scans/s (MCT detector), and using a resolution of 4 cm^{-1} . The background spectrum of the solid was taken under $10\text{ vol}\% \text{ H}_2\text{O}/\text{Ar}$ flow at the desired reaction temperature. The DRIFTS data are reported as $\log(1/R)$ (absorbance mode) using the relationship, $R = I/I_0$. Here, R is the catalyst sample reflectance, I_0 is the absorbance intensity of the solid itself, and I is the absorbance intensity of both the solid catalyst and the adsorbed species under reaction conditions. The function $\log(1/R)$ was found to give a better linear correlation of the integral band against surface coverage than that given by the Kubelka–Munk function for strongly absorbing media [53]. SSITKA-DRIFTS experiments with ^{13}CO (99.9 at% ^{13}C , Spectra Gases, Inc.) involved the switch 3 vol% $^{12}\text{CO}/10\text{ vol}\% \text{ H}_2\text{O}/\text{Ar}/\text{He}$ (T , 30 min) \rightarrow 3 vol% $^{13}\text{CO}/10\text{ vol}\% \text{ H}_2\text{O}/\text{Ar}$ (T , t) at a total flow rate of 200 N mL min^{-1} which potentially allows determining the chemical structure of the *active* intermediates and *spectator* species of the WGS reaction.

2.5. Probing “redox” versus “associative” WGS reaction mechanism

A novel experiment designed and performed which allowed the measurement of the initial rate of reaction of adsorbed formate and CO with water alone, where the surface concentrations of the former species were established under steady-state WGS reaction conditions was recently reported by us [16,17]. The experiment was slightly modified compared to that reported earlier [16,17], and it was as follows. After steady-state WGS reaction rate was obtained on the catalyst surface, the 3 vol% $^{12}\text{CO}/10\text{ vol}\% \text{ H}_2\text{O}/\text{Ar}$ feed gas stream was changed (step change) to a 3 vol% $^{12}\text{CO}/\text{Ar}$ gas mixture for 10 min in order to remove gas-phase water and keep the adsorbed CO on the catalyst surface. The feed was then replaced with an equivalent 3 vol% $^{13}\text{CO}/\text{Ar}$ gas mixture for 10 min in order to replace adsorbed ^{12}CO -s with ^{13}CO -s and leave on the catalyst surface non-exchangeable “carbon-containing” active intermediates (e.g., H^{12}COO (formate) and $^{12}\text{COOH}$ (carboxyl)) formed under WGS ($^{12}\text{CO}/\text{H}_2\text{O}/\text{Ar}$) reaction conditions. The feed was then changed to a $10\text{ vol}\% \text{ H}_2\text{O}/\text{Ar}$ gas and at the same time the transient responses of $^{12}\text{CO}_2$, $^{13}\text{CO}_2$ and H_2 were continuously monitored by *on line* mass spectrometer. The initial transient rates of $^{12}\text{CO}_2$ and $^{13}\text{CO}_2$ formation are considered as characteristic rates of the reaction of water with adsorbed non-exchangeable “carbon-containing”

and ^{13}CO -s intermediates, which allow discriminating the prevailing mechanism, e.g., “redox” versus “associative”. The shape and position in time of the $^{12}\text{CO}_2$ and $^{13}\text{CO}_2$ transient response curves obtained would reflect the kinetics of reaction of adsorbed non-exchangeable “ ^{12}C -containing” and ^{13}CO -s intermediates with water. In the present work, the above described experiment was conducted in the DRIFTS cell (83 mg of $\text{Pt}/\text{Ce}_{0.8}\text{La}_{0.2}\text{O}_2$ catalyst in powder form) in an *operando* mode, where DRIFTS spectra were collected under all steps of the above described gas delivery sequence.

2.6. $^{18}\text{O}/^{16}\text{O}$ isotope exchange followed by WGS reaction

$^{18}\text{O}/^{16}\text{O}$ isotopic exchange experiments were carried out in the same apparatus used for SSITKA-MS studies (Section 2.3). The catalyst sample (0.3 g) was first pre-treated with $10\text{ vol}\% ^{18}\text{O}_2/\text{Ar}$ (97% ^{18}O , Marshall Isotopes Ltd.) at 600°C for 30 min, purged with Ar and cooled to 80°C . The feed was then switched to H_2 (1 bar) at 80°C for 20 min to reduce only PtO_x to Pt^0 . Following this gas treatment, the catalyst was then heated from 80 to 250°C in Ar flow, and then exposed to the WGS reaction feed stream (3 vol% $\text{CO}/10\text{ vol}\% \text{ H}_2\text{O}/\text{Ar}$; 200 N mL min^{-1}). The $^{18}\text{O}/^{16}\text{O}$ isotopic exchange was monitored with mass spectrometry by recording the evolution of $^{16}\text{O}_2$, $^{16}\text{O}^{18}\text{O}$ and $^{18}\text{O}_2$ gaseous species ($m/z = 32, 34$ and 36), while mass numbers (m/z) 2 (H_2), 28 (C^{16}O), 44 (C^{16}O_2), 46 ($\text{C}^{16}\text{O}^{18}\text{O}$) and 48 (C^{18}O_2) were continuously monitored under the WGS reaction conditions.

3. Results and discussion

3.1. Catalyst characterization

Table 1 reports textural properties of the three $\text{Pt}/\text{Ce}_{1-x}\text{La}_x\text{O}_{2-\delta}$ ($x = 0.0, 0.2$ and 1.0) catalysts investigated in the present work. $\text{Pt}/\text{Ce}_{0.8}\text{La}_{0.2}\text{O}_{2-\delta}$ exhibits significantly higher specific surface area (SSA, $\text{m}^2\text{ g}^{-1}$) and smaller mean pores diameter (d_p , nm) compared to Pt supported on CeO_2 and La_2O_3 single metal oxides. However, the presence of mesoporosity is evidenced for all three materials with a mean pores diameter in the $4.1\text{--}9.3\text{ nm}$ range. Similar results were reported by Constantinou et al. [54] in their study of the effect of La^{3+} -dopant in $\text{Ce}_x\text{Zr}_{1-x}\text{O}_2$ on the redox properties of $\text{Ce}\text{--}\text{Zr}\text{--}\text{La}\text{--}\text{O}$ solid solution. In particular, it was reported that at the level of 4 at% La^{3+} -dopant concentration, the SSA increased by 53%.

Fig. 1a shows high angle annular dark field (HAADF) images (STEM mode) obtained on the fresh (after calcination in $20\text{ vol}\% \text{ O}_2/\text{He}$ at 600°C and H_2 reduction at 300°C) $0.5\text{ wt}\% \text{ Pt}/\text{La}_2\text{O}_3$ catalyst, whereas Fig. 1b the corresponding Pt particle size distribution estimated after counting about 200 particles, where a mean Pt particle size of $1.0 (\pm 0.3\text{ nm s.d.})$ was estimated. A similar relatively narrow Pt particle size distribution was obtained for the $0.5\text{ wt}\% \text{ Pt}/\text{CeO}_2$ and $0.5\text{ wt}\% \text{ Pt}/\text{Ce}_{0.8}\text{La}_{0.2}\text{O}_{2-\delta}$ catalysts, resulting in a mean Pt particle size of 1.2 and 1.0 nm , respectively (see Table 1). Based on EDS analyses in the region on top of Pt particles, no decoration effects of Pt by reducible CeO_x and LaO_x species were seen, in

Table 1

Textural properties, metal dispersion and mean platinum particle size of $\text{Pt}/\text{Ce}_{1-x}\text{La}_x\text{O}_{2-\delta}$ ($x = 0.0, 0.2$ and 1.0) catalysts.

Catalyst	BET ($\text{m}^2\text{ g}^{-1}$)	Mean pore size, d_p (nm)	Pt dispersion, D (%) ^a	Pt mean particle size (nm) ^b
$0.5\text{ wt}\% \text{ Pt}/\text{CeO}_2$	14.5	6.7	92	$1.2 (\pm 0.3\text{ s.d.})$
$0.5\text{ wt}\% \text{ Pt}/\text{Ce}_{0.8}\text{La}_{0.2}\text{O}_{2-\delta}$	42.0	4.1	100	$1.0 (\pm 0.2\text{ s.d.})$
$0.5\text{ wt}\% \text{ Pt}/\text{La}_2\text{O}_3$	7.0	9.3	100	$1.0 (\pm 0.3\text{ s.d.})$

^a Use of the formula: $D(\%) = 1.1/d_{\text{Pt}}(\text{nm}) \times 100$.

^b According to HAADF/STEM studies (e.g., Fig. 1).

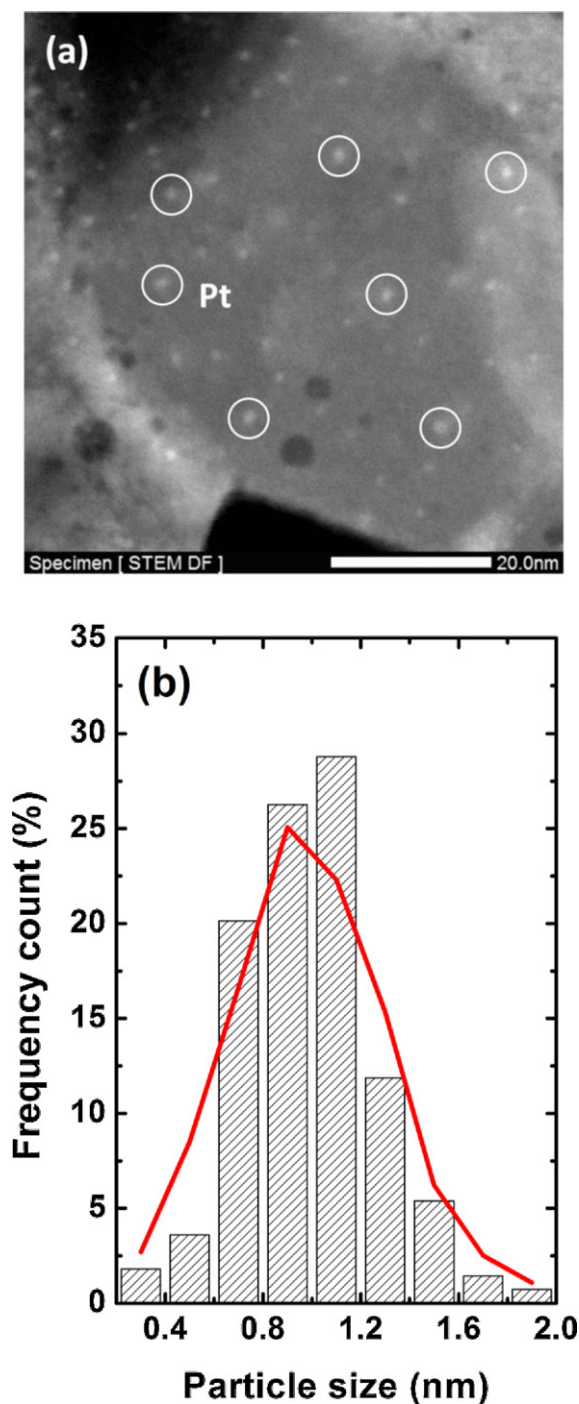


Fig. 1. (a) HAADF/STEM image and (b) Pt particle size distribution obtained over a 0.5 wt% Pt/La₂O₃ catalyst calcined at 600 °C in 20 vol% O₂/He and reduced in H₂ at 300 °C.

agreement to HRTEM images reported elsewhere [55] for hydrogen reduction temperatures below 500 °C. The STEM studies provided a Pt mean particle size similar to within 20% for all three supported Pt catalysts investigated. This result facilitates the interpretation of the effect of support chemical composition on the catalytic and mechanistic WGS reaction results to be presented next, which essentially should not be associated with any Pt particle size effects [16,17]. Based on the HAADF/STEM results, the dispersion of Pt was estimated, and this is reported also in Table 1.

Table 2

CO conversion (X_{CO} , %) obtained over the Pt/Ce_{1-x}La_xO_{2-δ} ($x=0.0, 0.2$ and 1.0) catalysts under steady-state WGS reaction conditions in the 250–325 °C range.

Catalyst	CO conversion (X_{CO} , %)			
	250 °C	275 °C	300 °C	325 °C
Pt/CeO ₂	24.9	41.5	64.0	76.8
Pt/Ce _{0.8} La _{0.2} O _{2-δ}	31.8	60.0	81.3	93.0
Pt/La ₂ O ₃	14.5	26.0	38.6	58.1

3.2. Catalytic activity measurements

Table 2 reports the catalytic activity performance of 0.5 wt% Pt/CeO₂, 0.5 wt% Pt/Ce_{0.8}La_{0.2}O_{2-δ} and 0.5 wt% Pt/La₂O₃ solids toward the WGS reaction in the 250–325 °C range in terms of CO conversion (X_{CO} , %). In all temperatures, the Pt/Ce_{0.8}La_{0.2}O_{2-δ} catalyst shows higher activity compared to Pt supported on CeO₂ and La₂O₃, especially at 275 and 300 °C where an increase by a factor of 1.3–2.3 is noted. It is mentioned here that Pt/CeO₂ is considered as one of the most effective catalysts for low-temperature WGS [30–32,56].

The intrinsic kinetic rate of the WGS reaction at 300 °C was also measured and expressed based on the length of the perimeter of the Pt–support interface ($\mu\text{mol CO cm}^{-1} \text{ s}^{-1}$) than on the Pt surface (TOF, s^{-1}). This analysis is meaningful since the mechanism of WGS reaction on the present catalytic systems involves active catalytic sites at the Pt–support interface and within a reactive zone around each Pt nanoparticle, as will be shown in the following Section 3.7. For each catalyst, the length of the perimeter of Pt–support interface, I_0 (cm g^{-1}) was estimated (Table 3) considering that each Pt nanoparticle has a hemispherical geometry, and accounting for the Pt loading and the corresponding mean Pt particle size (Table 1, Ref. [16]).

The specific kinetic rate per gram basis, r_{CO} ($\mu\text{mol CO g}^{-1} \text{ s}^{-1}$) and that based on I_0 , R_{CO} ($\mu\text{mol CO cm}^{-1} \text{ s}^{-1}$) at 300 °C estimated for each catalyst are reported in Table 3. It is seen that Pt nanoparticles of similar size supported on Ce_{0.8}La_{0.2}O_{2-δ} exhibit larger specific rate per length of Pt–support interface by a factor of 2.8 and 1.35, respectively compared to La₂O₃ and CeO₂ supports. This analysis of kinetic rates illustrates that the fact that Pt/Ce_{0.8}La_{0.2}O_{2-δ} specific rate expressed per gram of catalyst basis is the largest observed (see Tables 2 and 3) can be explained as due to differences in the site reactivity along the Pt–support interface largely influenced by the different support chemical composition. We have reported [16] that on Pt/CeO₂ active sites along the Pt–ceria interface, namely Pt–O–Ce and Ce³⁺–□–Ce³⁺, should possess different intrinsic site reactivity depending on the Pt particle size. As the Pt particle size decreases, Pt atoms with lower coordination and different local electron density are formed. This in turn influences the electron density on adjacent oxygen atoms of support. Another important intrinsic kinetic parameter which strongly influences the rate of reaction is the surface concentration of the active intermediates involved in the rate-limiting step of WGS. This kinetic parameter should also be considered in order to explain the differences observed in the specific reaction rate per gram basis of the three

Table 3

Effect of Ce/La ratio on the specific kinetic rate of WGS reaction per gram of catalyst, r_{CO} ($\mu\text{mol g}^{-1} \text{ s}^{-1}$), and per total length of perimeter of Pt–Ce_{1-x}La_xO_{2-δ} interface (I_0 , cm g^{-1}), R_{CO} ($\mu\text{mol cm}^{-1} \text{ s}^{-1}$) at 300 °C ($P_{\text{CO}} = 0.03$ bar, $P_{\text{H}_2\text{O}} = 0.1$ bar, $P_{\text{H}_2} = 0.87$ bar).

Catalyst	r_{CO} ($\mu\text{mol g}^{-1} \text{ s}^{-1}$)	I_0 (cm g^{-1})	R_{CO} ($\mu\text{mol cm}^{-1} \text{ s}^{-1}$)
0.5 wt% Pt/CeO ₂	6.2	1.9×10^{11}	3.2×10^{-11}
0.5 wt% Pt/Ce _{0.8} La _{0.2} O _{2-δ}	12.0	2.8×10^{11}	4.3×10^{-11}
0.5 wt% Pt/La ₂ O ₃	4.3	2.8×10^{11}	1.5×10^{-11}

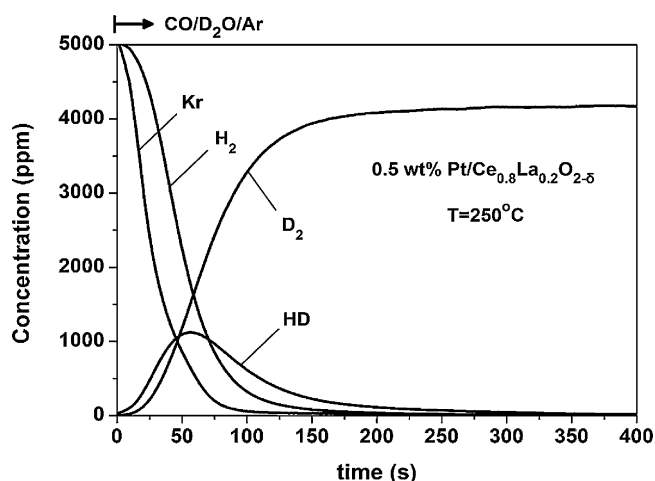


Fig. 2. SSITKA-mass spectrometry experiment performed to estimate the active “hydrogen-containing” (H-pool) reaction intermediates found in the WGS reaction path on 0.5 wt% Pt/Ce_{0.8}La_{0.2}O_{2-δ} at 250 °C. Gas delivery sequence: 3 vol% CO/10 vol% H₂O/Ar/Kr (30 min) → 3 vol% CO/10 vol% D₂O/Ar (t).

catalyst compositions. This subject is elaborated in Sections 3.3, 3.5 and 3.7.

3.3. SSITKA-mass spectrometry studies

3.3.1. Estimation of the concentration of active H-pool

SSITKA-mass spectrometry (MS) experiments to follow the hydrogen-path, named H-path of the WGS reaction mechanism from H₂O to the H₂ product gas followed the switch CO/H₂O/Ar/Kr (30 min, T) → CO/D₂O/Ar (T, t) at 250 and 300 °C (X_{CO} < 20%, Section 2.3). Fig. 2 presents transient concentration response curves of H₂, HD, D₂ and Kr obtained after the isotopic switch was made over the 0.5 wt% Pt/Ce_{0.8}La_{0.2}O₂ catalyst at 250 °C. The Kr response curve describes the hydrodynamic behavior of the flow-system from the chromatographic switching valve to the mass spectrometer (through the reactor with the catalyst bed in place), and accounts for the gas hold-up in the lines between the switching valve and the micro-reactor/MS analysis system, and the reactor volume [29,50]. The transient response curves (Fig. 2) were reproducible within 5% after performing consecutive switches between the CO/H₂O/Ar/Kr and CO/D₂O/Ar gas mixtures. The concentration of active “H-containing” intermediate species (H-pool) which are found in the H-path of WGS reaction mechanism is estimated based on the transient response curves of H₂, HD and Kr via the following relationship [16,19,51,52]:

$$N_H \left(\mu\text{mol H g}_{\text{cat}}^{-1} \right) = \left(\frac{F_T}{W} \right) \left[2 \int_0^{t^f} (y_{H_2} - y_{Kr}) dt + \int_0^{t^f} y_{HD} dt \right] \quad (1)$$

where, y_i is the molar fraction (mol%) of the gas-phase species i , F_T is the total molar flow rate (mol min⁻¹) at the reactor outlet, W is the mass of catalyst (g), and t^f is the time (min) required to obtain the new steady-state after the isotopic switch.

The H-pool ($\mu\text{mol H g}_{\text{cat}}^{-1}$) estimated is reported in Table 4 and is considered to be within 5% accuracy. The corresponding surface coverage of “hydrogen-containing” species (θ_H) based on the surface Pt atoms ($\mu\text{mol Pt}_s \text{ g}_{\text{cat}}^{-1}$) is also reported in Table 4 after using the estimated Pt dispersion (D , %) for each catalyst (Table 1). It is seen that in all cases $\theta_H \gg 1$, a result that strongly implies that the majority of these species must reside on the surface of support. The chemical nature of these active “H-containing” intermediates is considered to be largely of labile hydroxyls (–OH) on metal cations and atomic hydrogen (H) from water dissociation

Table 4

Concentration ($\mu\text{mol g}_{\text{cat}}^{-1}$) and surface coverage (θ_H) of active “H-containing” (H-pool) species of the WGS reaction over 0.5 wt% Pt/Ce_{1-x}La_xO_{2-δ} ($x = 0.0, 0.2$ and 1.0) catalysts measured by SSITKA-mass spectrometry experiments.

Catalyst	T (°C)	H-pool ($\mu\text{mol g}_{\text{cat}}^{-1}$)	θ_H
Pt/CeO ₂	300	285.6	12.1
Pt/Ce _{0.8} La _{0.2} O _{2-δ}	250	109.5	4.3
Pt/Ce _{0.8} La _{0.2} O _{2-δ}	300	408.5	15.9
Pt/La ₂ O ₃	300	353.0	13.8

attached on the surface oxygen anions (Oⁿ⁻) of support. It has been suggested [13,14,19,57] also that oxygen defect vacancies (\square_s) in partially reducible metal oxides (e.g., CeO₂, La₂O₃, TiO₂) can act as specific sites for H₂ activation. Formate (HCOO–) and carboxyl (–COOH) species could also be considered as active “H-containing” intermediates based on SSITKA-DRIFTS and other transient isotopic experiments to be presented in the following sections. The present results regarding the size of the H-pool find support from previous investigations made on Pt/γ-Al₂O₃ [51,52], Au/CeO₂ [46,58], Pt/TiO₂ [18,19] and Pt/CeO₂ [13,14,16–18,57] catalysts, where the presence of a reactive zone around each metal nanoparticle under steady-state WGS reaction conditions was suggested. Active species (e.g., –OH/H) may diffuse within this reactive zone and toward the metal–support interface, where in the latter case Pt metal sites are likely required for the formation of reaction products (e.g., formate/carboxyl reaction with atomic oxygen or di-hydrogen formation [42]). The importance of the extent of such a reactive zone around each Pt nanoparticle is further discussed in Section 3.5.

The formation of HD(g) shown in Fig. 2 might be also the result of recombination of adsorbed H and D on the Pt surface, and also of the exchange of H of –OH group of support with D from D₂(g) and/or D₂O(g) under the ¹²CO/D₂O/Ar gas switch. However, the latter side exchange reaction that leads to an overestimation of the H-pool was carefully checked according to our previous works [16–19]. It was found that this was very small, and practically it does not affect the size of the H-pool reported in Table 4. On the other hand, it should be pointed out that the reversibly adsorbed H or D on the Pt surface is included in the estimation of the concentration of H-pool since H₂(g) formation on Pt is expected to occur by the recombination of two adjacent adsorbed H species; adsorbed H on Pt is considered as a true active reaction intermediate.

Based on the SSITKA results reported in Fig. 2, the rate of H₂ formation under ¹²CO/H₂O/Ar is lower by a factor of 1.25 than the corresponding rate of D₂ formation obtained under ¹²CO/D₂O/Ar gas treatment. The latter result implies the existence of a normal kinetic isotopic effect (NKIE), which is related to the strength of chemical bond(s) involved in the rate-determining step (RDS). In the case of WGS reaction, one of the following steps could be considered as RDS: (i) water dissociation on the support (“redox” mechanism), (ii) formate (HCOO–) decomposition (“associative” mechanism) [42], and (iii) surface diffusion of H/OH species (breaking of O–H and Mⁿ⁺–OH bonds) within the reactive zone and toward the metal–support interface.

Ricote et al. [15] proposed that the rate-determining step (RDS) could be that of decomposition of HCOO– (formed on the support) on Pt to yield CO₂, whereas it was reported that water promotes the rate of WGS reaction on Pt/CeO₂ by the formation of –OH groups adjacent to the formate active intermediate, thus “a reactant promoted” mechanism was proposed [59]. However, according to Meunier et al. [28,45,46] and recent works from our laboratory [16–18], formate species was found to be inactive at $T < 200$ °C, whereas the “redox” mechanism on Pt/CeO₂ at $T > 250$ °C was found to predominate over the “associative formate with –OH group regeneration” mechanism; the latter is considered to operate in parallel with the “redox” mechanism but contributes to a lesser extent in the overall WGS reaction rate.

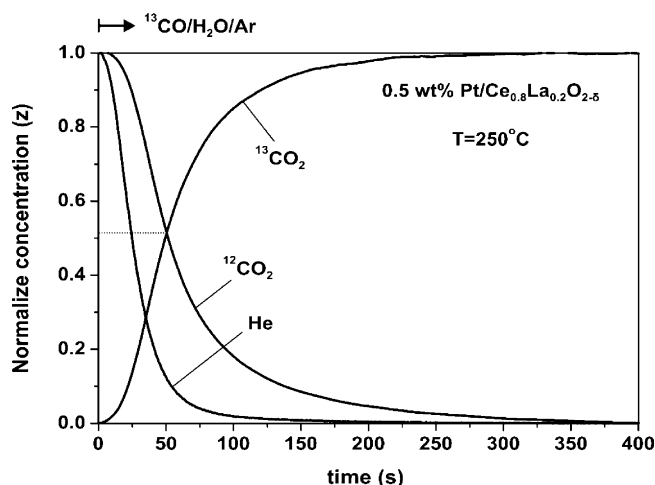


Fig. 3. SSITKA-mass spectrometry experiment performed to estimate the active “carbon-containing” (C-pool) reaction intermediates found in the WGS reaction path on 0.5 wt% Pt/Ce_{0.8}Zr_{0.2}O_{2-δ} at 250 °C. Gas delivery sequence: 3 vol% ¹²CO/10 vol% H₂O/Ar/He (30 min) → 3 vol% ¹³CO/10 vol% H₂O/Ar (t).

3.3.2. Estimation of the concentration of active C-pool

The SSITKA experiment using ¹³CO was performed following the switch ¹²CO/H₂O/Ar/He (30 min) → ¹³CO/H₂O/Ar (t) at 250 and 300 °C in order to record the transient evolution of all gaseous “carbon-containing” species as the result of the presence of active reaction intermediates found in the carbon-path of WGS (from CO to CO₂). Based on these transients, the concentration of only the active “carbon-containing” species, named C-pool is estimated. Fig. 3 shows transient response curves in terms of normalized concentration (Z) of ¹²CO₂(g), ¹³CO₂(g) and He obtained after the isotopic switch was made over the 0.5 wt% Pt/Ce_{0.8}La_{0.2}O_{2-δ} catalyst at 250 °C. Since the steady-state rates of ¹²CO₂ and ¹³CO₂ under the non-isotopic and isotopic CO/H₂O gas mixtures were the same, no ¹³C-isotopic kinetic effect was observed. An exponential-like decay of the ¹²CO₂ signal accompanied by an increase in ¹³CO₂ was observed. According to the SSITKA theory [29,50], the position of ¹²CO₂(g) and ¹³CO₂(g) transient response curves in time under the ¹³CO/H₂O switch must be such that the sum of the concentrations of ¹²CO₂ and ¹³CO₂ is equal to the steady-state concentration of ¹²CO₂ obtained under the ¹²CO/H₂O gas treatment [16–19]. In terms of the dimensionless concentration Z (Fig. 3), the sum of Z(¹²CO₂) and Z(¹³CO₂) must be equal to 1.0 at any time during the transient. The latter important criterion of the SSITKA experiment was fully satisfied since the two transient response curves cross each other at Z = 0.51 versus 0.50 (2% deviation).

The concentration (μmol C_{gcat}⁻¹) of C-pool participating in the carbon-path of the WGS reaction from CO to the CO₂ formation was estimated based on the following relationship [16,29,51,52]:

$$N_C(\mu\text{mol C}_{\text{gcat}}^{-1}) = \left(\frac{F_T}{W}\right) \left[\int_0^t (y_{\text{CO}_2} - y_{\text{He}}) dt \right] \quad (2)$$

The C-pool estimated over Pt/Ce_{1-x}La_xO_{2-δ} (x = 0.0, 0.2 and 1.0) as well as the corresponding equivalent surface coverage, θ_C (based on the Pt_s surface atoms) are given in Table 5. The C-pool is related to all active “C-containing” intermediates formed during WGS and which led to the CO₂(g) formation, such as adsorbed CO (CO_{ads}), carbonates ([CO₃]²⁻), formates (HCOO⁻) or carboxyl (—COOH) species. It is important to note that the ¹²CO₂(g) and ¹³CO₂(g) response curves are influenced by readsorption effects of CO₂ on active and non-active catalytic sites [29,60]. This effect was carefully considered after performing the experiments reported elsewhere

Table 5

Concentration (μmol g_{cat}⁻¹) and surface coverage (θ_C) of active “C-containing” (C-pool) species of the WGS reaction over 0.5 wt% Pt/Ce_{1-x}La_xO_{2-δ} (x = 0.0, 0.2 and 1.0) catalysts measured by SSITKA-mass spectrometry experiments.

Catalyst	T (°C)	C-pool (μmol g _{cat} ⁻¹)	θ _C ^a
Pt/CeO ₂	300	61.0	2.6
Pt/Ce _{0.8} La _{0.2} O _{2-δ}	250	71.8	2.8
Pt/Ce _{0.8} La _{0.2} O _{2-δ}	300	98.2	3.8
Pt/La ₂ O ₃	300	39.0	1.5

^a Based on HAADF/STEM studies (Fig. 1).

[16–18,29,60]. Thus, the concentration of C-pool reported in Table 5 is free of CO₂-readsorption effects.

In contrast to the large concentration of H-pool (Table 4), the concentration of C-pool in terms of θ_C is between 1.5 and 3.8 monolayers for all Pt/Ce_{1-x}La_xO_{2-δ} (x = 0.0, 0.2 and 1.0) catalysts (Table 5). These results strongly imply that the active “carbon-containing” intermediates are largely associated with sites along the platinum–support interface and within an active zone around each Pt nanoparticle (see Section 3.7). The possibility that part of it might be present on the Pt surface cannot be excluded. In fact, SSITKA-DRIFTS studies to be presented next provide evidence that active formate (HCOO⁻) and carboxyl (—COOH) species are formed on the Ce_{0.8}La_{0.2}O_{2-δ} metal oxide support and the Pt surface, and adsorbed CO on the Pt surface. In a recent work from our laboratory [16,17], it was proposed that active formate species reside along the periphery of Pt–ceria and Pt–Ce_{0.5}Zr_{0.5}O_{2-δ} support interface and on sites adjacent to that.

The concentration of C-pool reported in Table 5 can justify only an equivalent amount of the H-pool if it is considered that only active formate/carboxyl species participate in the carbon-path of WGS. However, the presence of molecularly adsorbed CO points out that the equivalent concentration of H-pool (Table 4) corresponding to HCOO⁻ and —COOH species must be less than the concentration of C-pool reported in Table 5. Thus, it becomes clear that the vast majority of H-pool (Table 4) consists of different in composition active “hydrogen-containing” intermediates, namely —OH/H as previously pointed out.

3.4. SSITKA-DRIFTS studies

SSITKA-DRIFTS studies performed in order to determine the chemical structure of active surface intermediates (e.g., adsorbed CO, formates, carboxyl or carbonates) that truly participate in the WGS reaction, and spectator species also formed during the same reaction are reported in Fig. 4. DRIFTS spectra recorded under the ¹²CO/H₂O feed stream at 250 °C on the 0.5 wt% Pt/Ce_{0.8}La_{0.2}O_{2-δ} catalyst in the 2250–1850 cm⁻¹ range, and which correspond to the C–O stretching vibrational mode of various types of Pt-bound CO, are presented in Fig. 4, upper spectrum. Deconvoluted and curve fitted spectra under both isotopic feed gas compositions are also shown. All spectra recorded under ¹²CO/H₂O steady-state reaction (30 min on stream) are presented by solid line, while deconvoluted ones corresponding to the ¹³CO/H₂O gas treatment (30 min) are presented by dashed line (bottom spectra).

The IR bands centered at 2182 and 2116 cm⁻¹, labeled as 1 and 2, respectively, are due to gas phase ¹²CO [61]. The low-intensity IR band centered at 2069 cm⁻¹ (band 3) is related to a high-frequency (HF) linearly bound CO on Pt, whereas the infrared band at 2046 cm⁻¹ (band 4) is assigned to a low-frequency (LF) linearly bound CO on Pt atoms present in small platinum particles (P_s) of low coordination (d_{Pt} < 15 Å) [16,62,63]. The IR band 5 recorded at 1995 cm⁻¹ is attributed to CO adsorbed on Pt sites of low coordination in very small particles (P_{VS}) [16,62–64]. Such Pt sites could be found at the periphery of metal–support interface. In general, linear CO adsorption does not lead to IR bands in this

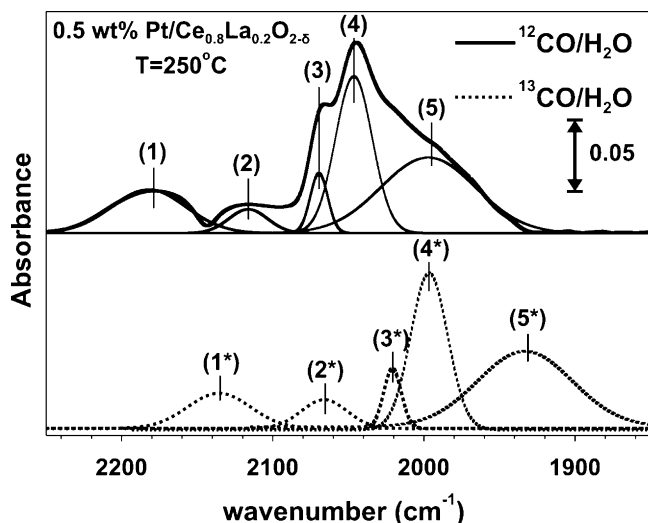


Fig. 4. SSITKA-DRIFTS spectra recorded in the 2250–1850 cm^{-1} range over 0.5 wt% Pt/Ce_{0.8}La_{0.2}O_{2-δ} under WGS reaction conditions at 250 °C. Solid-line spectra were recorded under 3 vol% ¹²CO/10 vol% H₂O/Ar/He and dashed-line spectra under 3 vol% ¹³CO/10 vol% H₂O/Ar feed gas mixtures. Deconvolution and curve fitting procedures of recorded DRIFTS spectra are also shown (IR bands 1–5 and 1*–5*).

spectral region. The substantial decrease of the $\nu(\text{CO})$ frequency could be explained by the electron transfer of an electron donor compound (e.g., La³⁺) toward platinum, which increases the back-donation of the metal electrons into the $2\pi^*$ antibonding orbital of adsorbed CO [63]. Another possible explanation is that introduction of La³⁺ into the ceria lattice facilitates reduction of the metal oxide ($\text{Ce}^{4+} \rightarrow \text{Ce}^{3+}$) resulting to an increase in the population of Ce³⁺-defect sites [26]. According to the discussion offered above, the low-frequency adsorbed CO IR band (1995 cm^{-1}) could be assigned to linear CO adsorbed on metallic Pt in contact with reduced Ce³⁺ located at the metal–support interface ($\text{Pt}-\square_s-\text{Ce}^{3+}$).

As depicted in Fig. 4 (bottom spectrum), all IR bands described above due to molecularly adsorbed CO show the *red isotopic shift* upon the switch $^{12}\text{CO}/\text{H}_2\text{O} \rightarrow ^{13}\text{CO}/\text{H}_2\text{O}$ (bands labeled with *). Based only on the observed red isotopic shift, it cannot be safely said that these species are all active intermediates as will be illustrated in Section 3.5. The latter implies that the isotopic shift observed could be due simply to the process of exchange of adsorbed ^{12}CO -s with $^{13}\text{CO}(\text{g})$. On the other hand, at least one adsorbed CO-s species must be considered as an *active intermediate* formed in the carbon-path of the WGS reaction, since CO is the only “C-containing” reactant species, in agreement with our previous studies [16–19,51]. In fact, it was proposed [16–19] that adsorbed CO on Pt reacts via the “redox” WGS reaction mechanism, where active sites are present in both the metal and support surfaces.

Characteristic νCH stretching mode IR bands recorded in the 3050–2750 cm^{-1} range (Fig. 5) are due to adsorbed formate species ($\text{HCOO}-$) formed under WGS at 250 °C on Pt/Ce_{0.8}La_{0.2}O_{2-δ}. The IR bands centered at 2940, 2890 and 2843 cm^{-1} (Fig. 5, upper spectrum) observed under $^{12}\text{CO}/\text{H}_2\text{O}$ reaction conditions correspond to the νCH , $\delta\text{CH} + \nu\text{OCO}_{\text{asym}}$ and $\delta\text{CH} + \nu\text{OCO}_{\text{sym}}$ vibrational modes of adsorbed $\text{HCOO}-$. The site location for the formation of the latter species, e.g., Pt versus Ce_{0.8}La_{0.2}O_{2-δ} metal oxide support, is difficult to be resolved based only on the resulting position of IR bands [13,15,37,61,65–67]. A strong indication that *active* $\text{HCOO}-$ reside on the support is only provided by the surface concentration of this species. For example, if θ_{HCOO} (based on Pt_s) is estimated to be greater than one then part of this active species is formed on the support surface, and the concept of having an *active reaction zone* around each Pt nanoparticle can be established (see Sections 3.5 and 3.7).

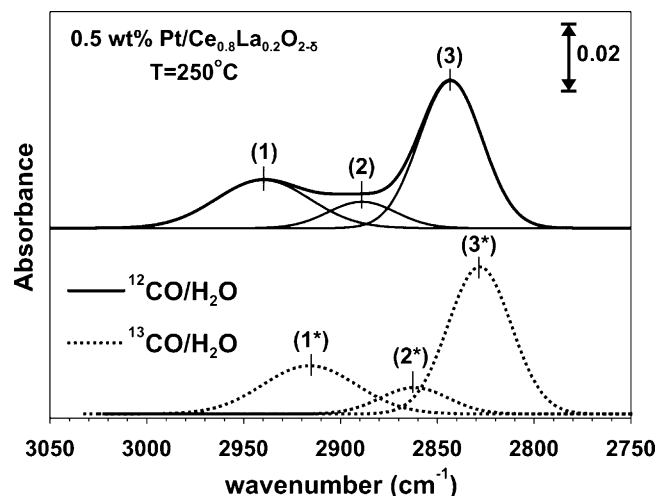


Fig. 5. SSITKA-DRIFTS spectra recorded in the 3050–2750 cm^{-1} range over 0.5 wt% Pt/Ce_{0.8}La_{0.2}O_{2-δ} under WGS reaction conditions at 250 °C. Solid-line spectra were recorded under 3 vol% ¹²CO/10 vol% H₂O/Ar/He and dashed-line spectra under 3 vol% ¹³CO/10 vol% H₂O/Ar feed gas mixtures. Deconvolution and curve fitting procedures of recorded DRIFTS spectra are also shown (IR bands 1–3 and 1*–3*).

Fig. 6 shows DRIFTS spectra in the 1700–1150 cm^{-1} region associated with the stretching (symmetric and anti-symmetric) vibrational modes of the O–C–O group of adsorbed carbonate, formate ($\text{HCOO}-$) and carboxyl ($-\text{COOH}$) species formed under WGS reaction conditions. The IR bands recorded at 1580 (band 1) and 1353 cm^{-1} (band 4) under the $^{12}\text{CO}/\text{H}_2\text{O}$ gas mixture (Fig. 6, upper spectrum) are assigned to OCO_{as} and OCO_{s} vibrational modes of formate (bidentate and bridged), carboxyl, and bicarbonate, whereas those centered at 1515 (band 2) and 1468 cm^{-1} (band 3) to carboxyl and polydentate carbonate, respectively [61].

After the new steady-state under the isotopic gas mixture of $^{13}\text{CO}/\text{H}_2\text{O}$ was reached, all the observed IR bands under $^{12}\text{CO}/\text{H}_2\text{O}$ gave the red isotopic shift; replacement of ^{12}C with ^{13}C in the carbon-path of the WGS (Figs. 5 and 6, bottom dashed-line spectra). SSITKA-DRIFTS spectra were also recorded over Pt/CeO₂ and Pt/La₂O₃ catalysts at 250 and 300 °C, where no additional IR bands that could be assigned to different adsorbed species except those observed on Pt/Ce_{0.8}La_{0.2}O_{2-δ} (Figs. 4–6) were noticed.

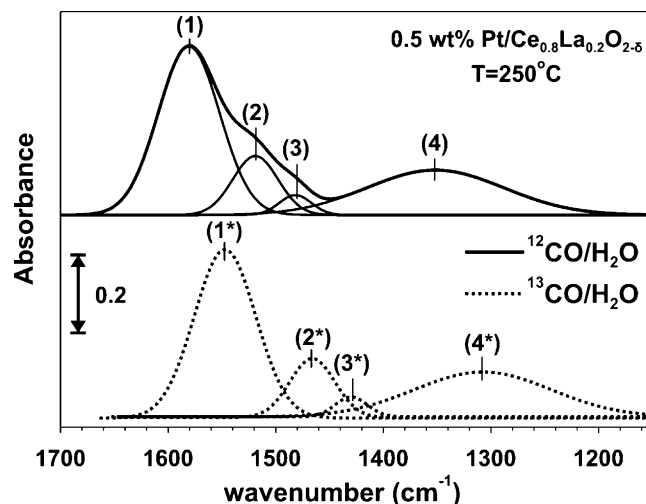
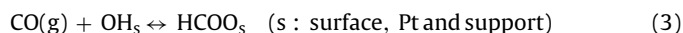


Fig. 6. SSITKA-DRIFTS spectra recorded in the 1700–1150 cm^{-1} range over 0.5 wt% Pt/Ce_{0.8}La_{0.2}O_{2-δ} under WGS reaction conditions at 250 °C. Solid-line spectra were recorded under 3 vol% ¹²CO/10 vol% H₂O/Ar/He and dashed-line spectra under 3 vol% ¹³CO/10 vol% H₂O/Ar feed gas mixtures. Deconvolution and curve fitting procedures of recorded DRIFTS spectra are also shown (IR bands 1–4 and 1*–4*).

The above described SSITKA-DRIFTS results lead to the conclusion that *at least one* of the formate, carbonate or carboxyl adsorbed species formed on the metal and/or support surfaces is found in the carbon-path of the WGS reaction mechanism, since all these species provided the red isotopic shift. Adsorbed CO should be considered as a precursor intermediate for the formation of formate, carbonate or carboxyl, and, therefore, *at least one* of the observed linear adsorbed CO on Pt (Fig. 4) must be also considered as an *active* reaction intermediate. On the other hand, we have previously reported [51] that if the reaction step of adsorbed CO with $-\text{OH}$ groups is a reversible step, and considering that $\text{H}^{12}\text{COO}-$ species does not further react to produce CO_2 and H_2 (*inactive* or *spectator*), then during the $^{13}\text{CO}/\text{H}_2\text{O}$ switch formate is expected to be labeled as $\text{H}^{13}\text{COO}-$. The same reasoning also applies for the formation of carboxyl species according to the work of Grabow et al. [42]. In the case of carbonate species, the red isotopic shift could be related either to CO_2 readsorption on true active or inactive catalytic sites, where part of carbonate species formed under WGS is reversibly chemisorbed, or to carbonates that could be considered as active intermediates based on a “redox” mechanism [18]. Meunier et al. [46] have determined the decomposition reaction rate of formate toward CO_2 formation under WGS reaction conditions over $\text{Au}/\text{Ce}(\text{La})\text{O}_2$ catalyst and compared this to the overall WGS reaction rate. Given that the former rate was found to be small, formate was excluded from being considered as a major reaction intermediate.

3.5. Probing the participation of formate, carboxyl and carbonate species in the carbon-path of WGS via transient isotopic water reactivity experiments

Fig. 7 reports DRIFT spectra recorded in the $1100\text{--}3000\text{ cm}^{-1}$ range under the 10 vol% $\text{H}_2\text{O}/\text{Ar}$ gas switch (100 mL min^{-1}) following the gas delivery sequence $^{12}\text{CO}/\text{H}_2\text{O}$ (30 min) \rightarrow $^{12}\text{CO}/\text{Ar}$ (10 min) \rightarrow $^{13}\text{CO}/\text{Ar}$ (10 min) \rightarrow $\text{H}_2\text{O}/\text{Ar}$ (t) performed isothermally at 250°C over the 0.5 wt% $\text{Pt}/\text{Ce}_{0.8}\text{La}_{0.2}\text{O}_{2-\delta}$ catalyst (see Section 2.5). Fig. 7a reports spectra in the characteristic region of νCH stretching vibrational mode due to formate ($\text{HCOO}-$) adsorbed species only (considering the likely adsorbed reaction intermediates of WGS). The spectrum marked with $t = 0\text{ s}$ corresponds to that recorded just after the 10-min $^{13}\text{CO}/\text{Ar}$ gas treatment of the catalyst, where the red isotopic shift for the observed IR bands was noted. According to the experiment performed, this result strongly indicates that the formation elementary step(s) of formate that involves $\text{CO}(\text{g})$ is reversible, as indicated by the following overall chemical equation:



Within 5 min in $\text{H}_2\text{O}/\text{Ar}$ gas stream, practically all adsorbed formate was depleted (Fig. 7a). It is important to note here that in another experiment, following the switch $\text{CO}/\text{H}_2\text{O}$ (30 min, 250°C) \rightarrow Ar (250°C , t), only a small decrease in the intensity of formate's IR bands was noticed after 10 min in Ar (inert gas) flow. This result demonstrates that practically the rate of decomposition of formate in Ar flow is practically very small at 250°C over the present catalytic system. Therefore, the results of Fig. 7a strongly suggest that depletion of formate surface concentration is largely due to the presence of water. This depletion of formate concentration leads to CO_2 and H_2 gases as evidenced by the mass spectrometer analysis performed (*operando* methodology) to be presented next. It is suggested that under $\text{H}_2\text{O}/\text{Ar}$ treatment, the formation of OH/H species on Pt and/or Pt-support interface after the removal by reaction of adsorbed CO on Pt enhances the rate of formate decomposition/reaction into CO_2 and H_2 , as evidenced also by previous works [16,40,42,56,59,67].

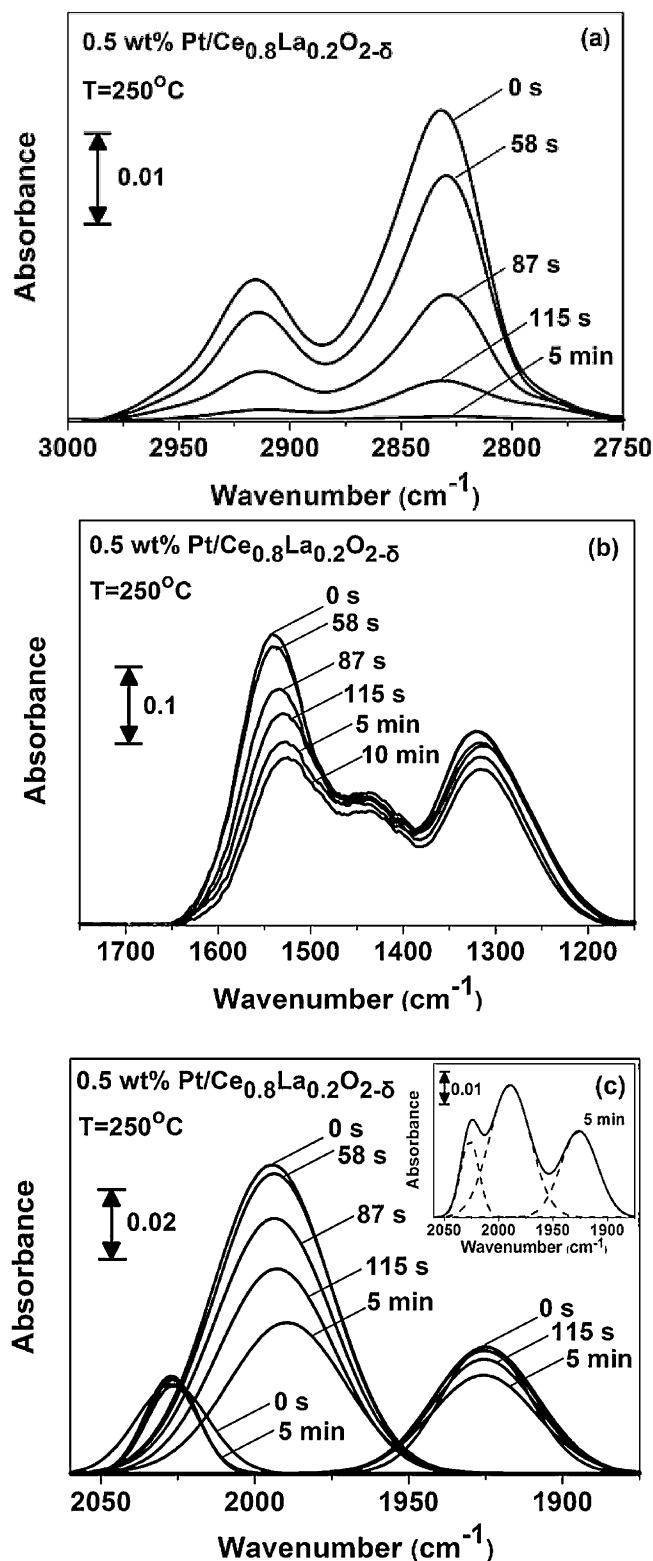


Fig. 7. DRIFTS spectra recorded over the 0.5 wt% $\text{Pt}/\text{Ce}_{0.8}\text{La}_{0.2}\text{O}_{2-\delta}$ catalyst at 250°C under the 10 vol% $\text{H}_2\text{O}/\text{Ar}$ (t) switch of the following gas delivery sequence: 3 vol% $^{12}\text{CO}/10\text{ vol}\%\text{H}_2\text{O}/\text{Ar}$ (30 min) \rightarrow 3 vol% $^{12}\text{CO}/\text{Ar}$ (10 min) \rightarrow 3 vol% $^{13}\text{CO}/\text{Ar}$ (10 min) \rightarrow 10 vol% $\text{H}_2\text{O}/\text{Ar}$ (t).

Fig. 7b presents similar DRIFT spectra recorded in the 1150–1700 cm^{-1} range. As previously mentioned (Fig. 6), the apparently three IR bands observed (Fig. 7b) were assigned to four individual bands after deconvolution and curve fitting. It was found that after 10 min in $\text{H}_2\text{O}/\text{Ar}$ flow the intensity of these IR bands did not change (Fig. 7b), strongly suggesting that part of these species is stable under water reactive conditions. Given the fact that formate (HCOO^-) species is all able to react under $\text{H}_2\text{O}/\text{Ar}$ stream after 10 min on stream (Fig. 7a), and that carboxyl intermediates (COOH^-) formed on Pt are even more reactive than formate species [42], it can be concluded that carbonate-type species should not consist part of the active C-pool of the WGS reaction (spectator species). The fact that all IR bands in the SSITKA-DRIFTS (Fig. 6) gave the red isotopic shift along with what was previously mentioned strongly implies that carbonate-type species reversibly interact with gaseous CO_2 . The inability of carbonate-type adsorbed species to react with water was proved also by a separate DRIFTS experiment. After 985 ppm CO_2/He gas treatment (30 min, 250°C) of the catalyst, the feed was changed to an Ar gas flow for 5 min, and then to 10 vol% $\text{H}_2\text{O}/\text{Ar}$ (250°C , t). No change in the IR bands intensity was seen under the latter gas switch.

Fig. 7c presents similar transient DRIFT spectra for the region of adsorbed CO after deconvolution and curve fitting. In the inset of Fig. 7c, the spectra before and after deconvolution corresponding to 5 min in $\text{H}_2\text{O}/\text{Ar}$ gas treatment are provided. It is observed that after 5 min in $\text{H}_2\text{O}/\text{Ar}$ gas stream there were refractory adsorbed CO species toward water for all three kinds of adsorbed CO (see Fig. 4). The most refractory were the HF-linear adsorbed CO on Pt and adsorbed CO on Pt sites of low coordination (see Section 3.4). On the other hand, the least refractory was the LF-linear CO associated with small Pt clusters ($d_{\text{Pt}} < 1.5 \text{ nm}$), where about half of its surface coverage reacted toward CO_2 and H_2 under the $\text{H}_2\text{O}/\text{Ar}$ gas atmosphere (Fig. 7c, IR band at 1994 cm^{-1}). It should be noted that all three kinds of adsorbed CO gave the red isotopic shift under the $^{13}\text{CO}/\text{Ar}$ gas treatment (reversible chemisorption). These results provide important information regarding the process of surface diffusion of CO from the Pt to the Pt-support interface and further to the support surface to form formate and carboxyl intermediates. It could be suggested (Fig. 7c) that the pathway of CO diffusion on Pt is partly blocked for a significant amount of CO, likely due to coadsorption with other species, such as OH, $-\text{COOH}$ and HCOO^- . Alternatively, part of adsorbed CO on Pt is not able energetically to react with water.

Fig. 8 shows the corresponding transient isotopic response curves of $^{12}\text{CO}_2$, $^{13}\text{CO}_2$ and H_2 obtained with mass spectrometry under the 10 vol% $\text{H}_2\text{O}/\text{Ar}$ switch in the *operando* mode DRIFTS-MS experiment describe above (Fig. 7, Section 2.5). It is clearly illustrated that most of CO_2 formed is $^{13}\text{CO}_2$ (54.7 $\mu\text{mol/g}$, or $\theta=2.1$) with only a small amount of $^{12}\text{CO}_2$ (5.4 $\mu\text{mol/g}$, or $\theta=0.2$). This amount of C-pool formed under $^{12}\text{CO}/\text{H}_2\text{O}$ treatment agrees well with that estimated under SSITKA-MS (Fig. 3, Table 5, $\theta=2.8$). The small difference is due to the fact that during this transient experiment some of the CO_2 formed is adsorbed irreversibly on the catalyst surface. In the case of hydrogen formation response, this corresponds to 50 $\mu\text{mol/g}$. This amount is the contribution of $-\text{COOH}$ and HCOO^- species found in the C-pool and which reacted under $\text{H}_2\text{O}/\text{Ar}$ (Fig. 7a and b) (2 mol of $-\text{COOH}$ or HCOO^- corresponds to 1 mol H_2), and of adsorbed CO (Fig. 7c; 1 mol CO corresponds to 1 mol H_2). As previously mentioned, adsorbed CO, HCOO^- and likely $-\text{COOH}$ reversibly interact with adsorbed CO. Therefore, the transient $^{13}\text{CO}_2$ response curve depicted in Fig. 8 is due to the reaction of these adsorbed species under $\text{H}_2\text{O}/\text{Ar}$ gas atmosphere. The fact that a single symmetrical $^{13}\text{CO}_2$ peak is observed (Fig. 8) may reasonably suggest that the kinetic rate of reaction of adsorbed CO and formate/carboxyl with water are similar. The small $^{12}\text{CO}_2$ response obtained with its peak maximum

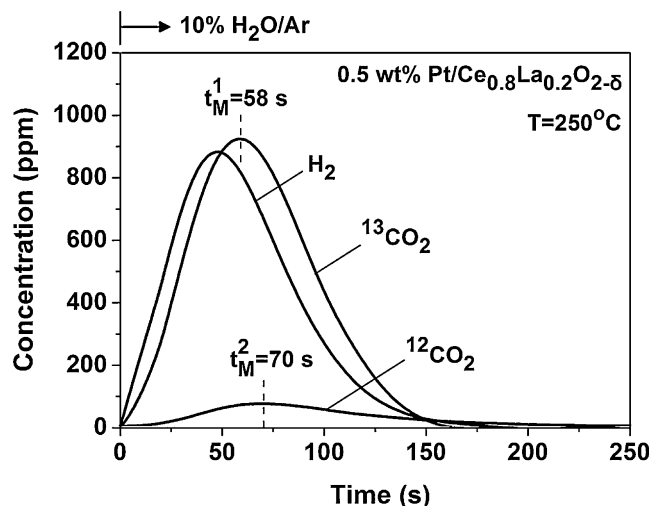


Fig. 8. Transient isothermal response curves of H_2 , $^{12}\text{CO}_2$ and $^{13}\text{CO}_2$ obtained on the 0.5 wt% Pt/ $\text{Ce}_{0.8}\text{La}_{0.2}\text{O}_{2-\delta}$ catalyst according to the following gas delivery sequence at 250°C : 3 vol% $^{12}\text{CO}/10 \text{ vol}\% \text{H}_2\text{O}/\text{Ar}$ (30 min) \rightarrow 3 vol% $^{12}\text{CO}/\text{Ar}$ (10 min) \rightarrow 3 vol% $^{13}\text{CO}/\text{Ar}$ (10 min) \rightarrow 10 vol% $\text{H}_2\text{O}/\text{Ar}$ (t).

shifted to higher reaction times compared to that of $^{13}\text{CO}_2$ peak is due to the presence of a small concentration of formate and/or carboxyl that react slowly with water, and which are irreversibly formed by the interaction of CO with $-\text{OH}$ groups (no exchange with ^{13}CO). This small concentration was not possible to be seen in the DRIFTS spectrum reported in Fig. 5 after deconvolution, and also in Fig. 7a.

3.6. Probing the “redox” mechanism in WGS over Pt/ $\text{Ce}_{0.8}\text{La}_{0.2}\text{O}_{2-\delta}$

Fig. 9a reports the ^{18}O -isotopic exchange occurred at 600°C in the 0.5 wt% Pt/ $\text{Ce}_{0.8}\text{La}_{0.2}\text{O}_{2-\delta}$ catalyst according to the experiment described in Section 2.6. Based on the $^{16}\text{O}_2$ and $^{16}\text{O}^{18}\text{O}$ transient response curves obtained, the total amount of exchangeable surface and bulk ^{16}O lattice oxygen was found to be 16.1 mmol/g. Upon the switch to the WGS reaction gas mixture at 250°C (see Section 2.6), the amount of ^{18}O lattice oxygen used to form C^{18}O_2 and $\text{C}^{16}\text{O}^{18}\text{O}$ based on the transient response curves reported in Fig. 9b (30 min in WGS reaction) was estimated to be 0.74 mmol/g. In order to prove that the production of C^{18}O_2 and $\text{C}^{16}\text{O}^{18}\text{O}$ under the WGS reaction is due largely to the reaction of adsorbed CO with the ^{18}O lattice oxygen of support (redox mechanism) and not by the simple exchange of $\text{C}^{16}\text{O}_2(\text{g})$ produced under WGS with the ^{18}O lattice oxygen of support, the following experiment was designed and performed. The catalyst was first calcined in $20\% \text{O}_2/\text{He}$ at 600°C for 2 h, reduced in H_2 at 300°C and then purged in He flow at 300°C . The following gas delivery sequence was then applied: 10 vol% $^{18}\text{O}_2/\text{Ar}$ (600°C , 30 min) \rightarrow Ar, cool down to $100^\circ\text{C} \rightarrow$ 1 atm H_2 (30 min, 100°C) \rightarrow Ar (20 min, 250°C) \rightarrow 985 ppm $\text{C}^{16}\text{O}_2/\text{Ar}$ (250°C , t). Fig. 9c presents all three isotopic carbon dioxide transient response curves obtained upon the 985 ppm $\text{C}^{16}\text{O}_2/\text{Ar}$ (250°C , t) gas treatment. It is clearly seen that the transient kinetics of isotopic exchange of ^{18}O lattice oxygen with C^{16}O_2 is totally different from the transient behavior of the rate of formation of these carbon dioxide isotopic species due to the reaction of lattice ^{18}O with CO under WGS reaction conditions (Fig. 9b). In particular, the maximum rate of formation of $\text{C}^{18}\text{O}^{18}\text{O}$ is obtained at 110 s after the $\text{CO}/\text{H}_2\text{O}$ switch (Fig. 9b), similar to the $^{13}\text{CO}_2$ formation depicted in Fig. 8, whereas that of simple exchange of C^{16}O_2 with ^{18}O lattice oxygen

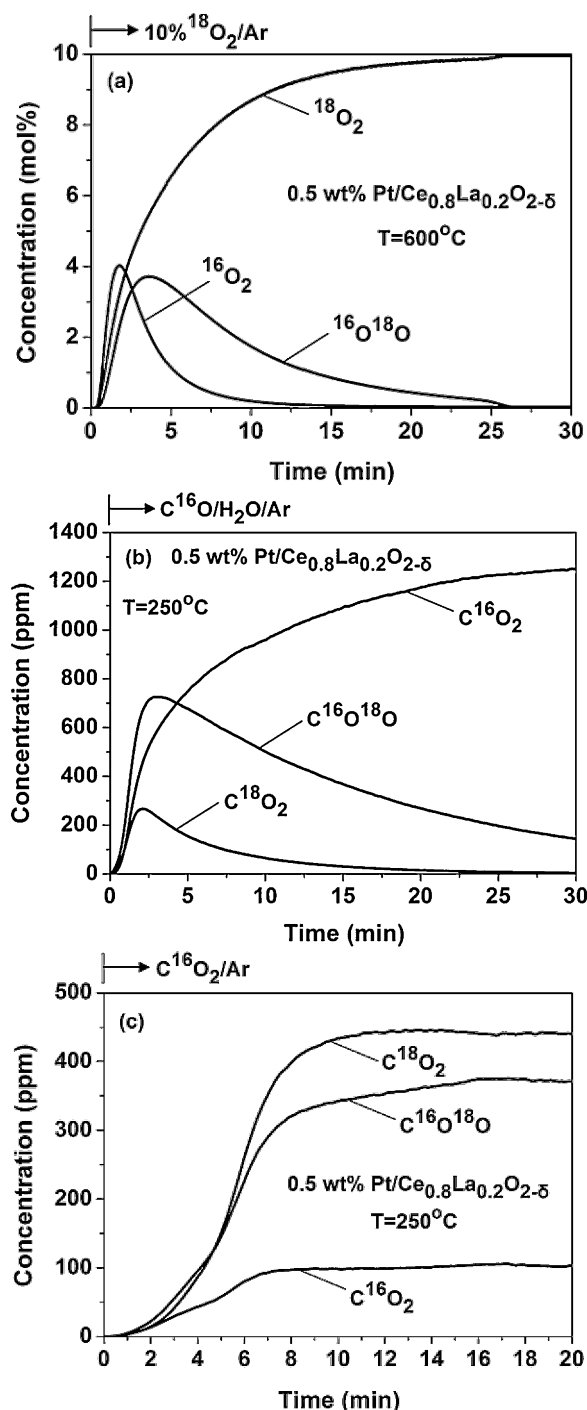


Fig. 9. (a) Transient response curves of ¹⁶O₂, ¹⁶O¹⁸O and ¹⁸O₂ obtained during the switch Ar → 10 vol% ¹⁸O₂/Ar at 600 °C; (b) Transient response curves of C¹⁶O₂, C¹⁶O¹⁸O and C¹⁸O₂ obtained during the switch to the WGS reaction gas mixture following (a) and the gas sequence described in Section 2.6; (c) Transient response curves of isotopic CO₂s recorded at 250 °C under the C¹⁶O₂/Ar flow according to the gas delivery sequence: 10 vol% ¹⁸O₂/Ar (600 °C, 30 min) → Ar, cool down to 100 °C → 1 atm H₂ (30 min, 100 °C) → Ar (20 min, 250 °C) → 985 ppm C¹⁶O₂/Ar (250 °C, t).

of support was observed at much larger times ($t=14\text{--}16\text{ min}$, Fig. 9c). Based on these results it is clear that the WGS reaction proceeds via the *redox* mechanism in parallel to the associative mechanism via formate and carboxyl intermediates, as also suggested by the previous transient isotopic experiment depicted in Fig. 8.

3.7. Effects of La³⁺-doping of ceria on the kinetics and mechanism of WGS on Pt/Ce_{1-x}La_xO_{2-δ} catalysts

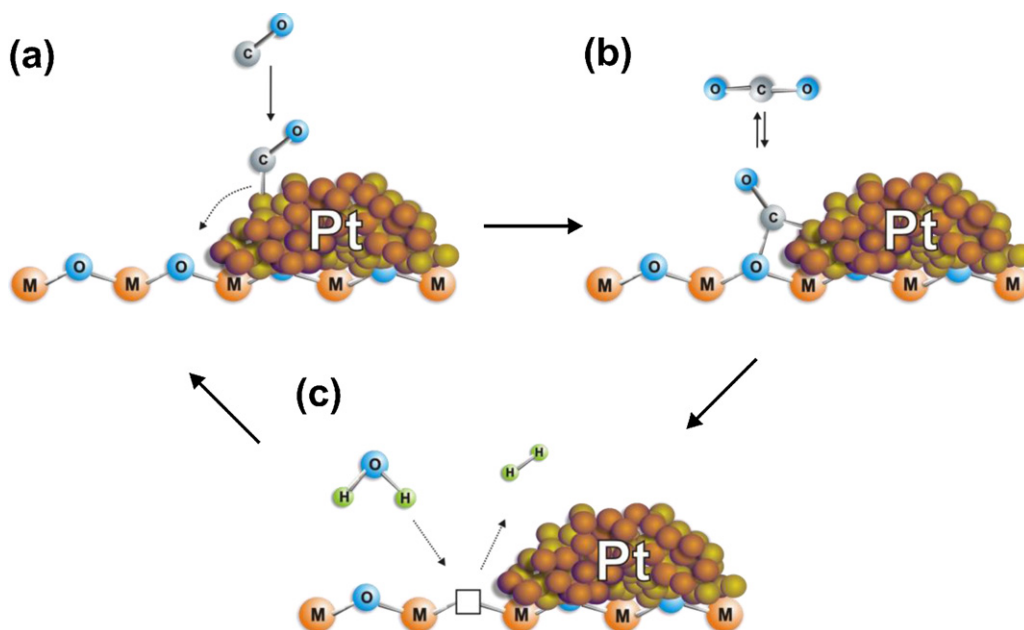
The effects of La³⁺-doping of ceria on (i) the *chemical composition*, (ii) *surface concentration* of active reaction intermediates found in the H-path and C-path of WGS, (iii) *extent of reaction zone* around each Pt nanoparticle, and (iv) the *prevailing mechanism* (“redox” versus “associative”) of WGS reaction are discussed in the present section.

The magnitude of surface concentration of H-pool (Table 4), an important kinetic parameter discussed in Section 3.3.1, along with the very small activity of ceria [16] and Ce_xLa_{1-x}O_{2-δ} ($x=0$ and 0.8) supports alone (not reported here), strongly suggest for the contribution of both the metal oxide support and Pt on the reaction sequence of steps. In addition, as clearly illustrated in Fig. 9, the “redox” mechanism (Scheme 1) extensively discussed in the literature [16–19,30–35,46,68] also applies in the present catalytic system. The second mechanism, that of “associative” [36–42,51] or “associative with OH group regeneration” [16,17] via formate and/or carboxyl active intermediate have been also discussed. The transient *operando* DRIFTS-MS isotopic experiments reported in Figs. 7a, b and 8 (Section 3.5) were very informative as to the participation of active formate and carboxyl intermediates in the reaction path of WGS via the “associative” route.

As illustrated in Scheme 1, adsorbed CO on Pt diffuses on a site adjacent to an oxygen atom along the metal–support interface, where it can react with surface lattice oxygen (“redox” mechanism) to form CO₂. Finally, water adsorbs and dissociates mainly on the partially reduced support sites (e.g., Ce³⁺–□_s) forming H₂(g), whereas the former gets re-oxidized. Grabow et al. [42] suggested a “redox” mechanism on Pt(111), where the active oxygen is provided by the dissociative chemisorption of water on the Pt surface. Also, the same authors reported that the “associative” route proceeds via a *carboxyl* than formate intermediate (spectator species). The results of the present work are not in contradiction to the latter findings, since as previously discussed, it is difficult with IR to discriminate the site location (Pt versus support) of formate and carboxyl species. However, the importance of the present work is that it proved that when Pt clusters (1.0–1.2 nm) are deposited on CeO₂, La₂O₃ or Ce_{0.8}La_{0.2}O_{2-δ}, formate and carboxyl species become active intermediates (Figs. 5–8).

When more than one reaction path is possible in a given catalytic reaction mechanism, then naturally the question arises as to what extent (% participation) each reaction path contributes to the overall kinetic rate observed. In our previous publications [16,17], based on the initial rates of ¹³CO₂ and ¹²CO₂ observed in the transient isotopic experiment depicted in Fig. 8, and the fact that during the ¹³CO/Ar gas treatment at 250 °C the formate (HCOO–) infrared bands have not provided the red isotopic shift, it was concluded that the “redox” mechanism prevailed over Pt/CeO₂ and Pt/Ce_{0.5}Zr_{0.5}O₂ catalysts. In the present work, the experimental results depicted in Figs. 7a, b and 8 as previously discussed in detail, support the view that both “redox” and “associative” reaction mechanism must be important for controlling the overall WGS reaction rate over Pt supported on Ce_{0.8}La_{0.2}O_{2-δ} solid solution.

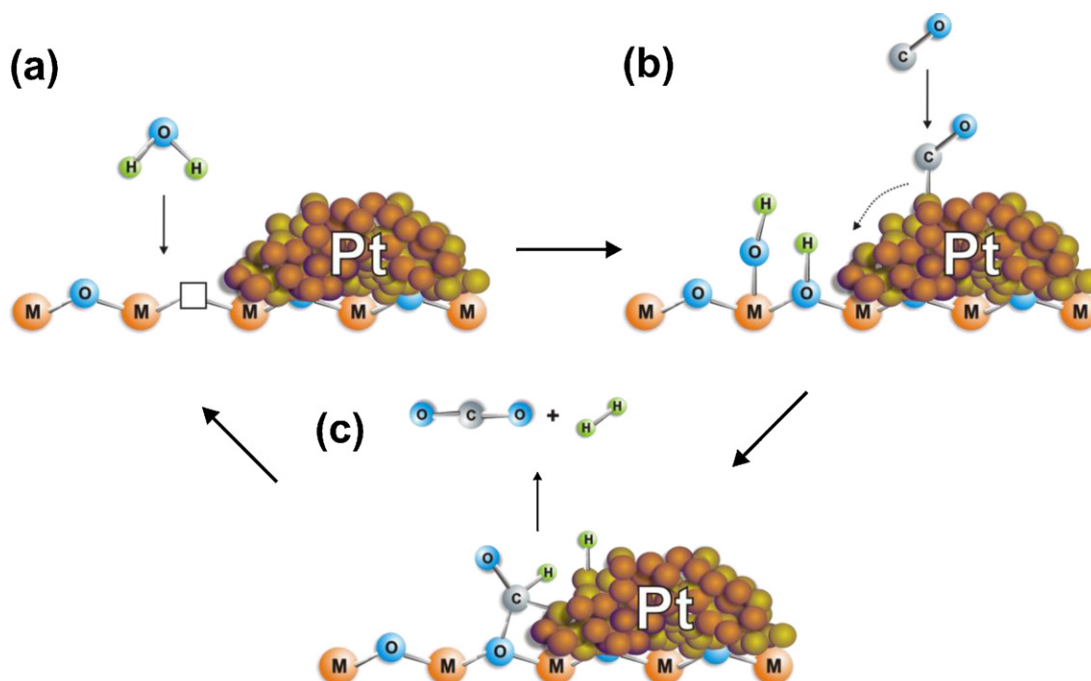
As previously discussed (Section 3.3.1, Table 4), the chemical nature of the majority of active “H-containing” (H-pool) intermediates should be considered that of labile hydroxyls (–OH) and atomic hydrogen (H), the latter attached on surface oxygen anions (Oⁿ⁻) of support and/or the Pt surface [42]. It has been suggested [13,57,69] that oxygen vacancies (□_s) in partially reducible metal oxides such as Ce_{1-x}La_xO_{2-δ} can act as specific sites for H₂ activation. Evidence for the presence of such sites at the metal–support interface (Pt–□_s–Ce³⁺ sites) is provided by the appearance of the LF-linear CO band (1998 cm⁻¹, Fig. 3).



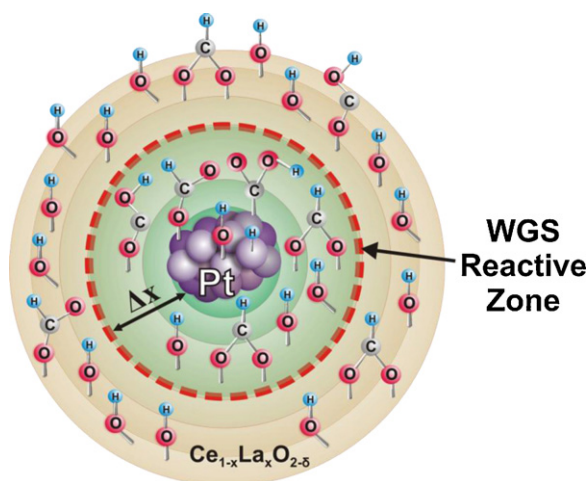
Scheme 1. Proposed "redox" mechanism operated in the WGS reaction over Pt/Ce_{1-x}La_xO_{2-δ} catalysts ($x=0.0, 0.2$ and 1.0); M = Ce⁴⁺ or La³⁺.

The "associative formate" mechanism for the WGS was considered to operate on *supported* Pt catalysts according to many previous works [13,44,70–72]. However, in all these studies no attempts were made to measure in situ the relative rates of WGS reaction at steady-state [46] or at the beginning of reaction (initial rates) [16,17] in order to provide strong support as to which mechanism prevails. The "associative formate with –OH group regeneration" mechanism (Scheme 2) is the combination of the two mechanistic paths largely proposed in the literature ("redox" and "associative formate"), and which is suggested to operate on the present Pt/Ce_xLa_{1-x}O_{2-δ} catalysts based on the present SSITKA (Figs. 4–6) and the transient isotopic reactivity with water

DRIFTS-MS experiments (Figs. 7 and 8) performed, and on previous findings [16,17]. According to Scheme 2, water dissociation proceeds on the M–□_s site (M = La³⁺ or Ce³⁺) leading to the formation of two hydroxyl groups (Scheme 2a,b), whereas formate intermediate is formed via the participation of adsorbed CO on Pt and –OH of support at the Ce_{1-x}La_xO_{2-δ}–Pt interface (Scheme 2c) or within a "reactive zone" around each Pt nanoparticle (see below). Formate species with the interaction of an adjacent adsorbed H (or –OH) on Pt decompose, producing CO₂(g) and H₂(g) and leaving oxygen vacancies on the Ce_xLa_{1-x}O_{2-δ} support to close the catalytic cycle. The concentration of oxygen vacancies is controlled by the rate of their formation via the reaction of adsorbed CO on Pt with labile



Scheme 2. Proposed "associative formate with –OH group regeneration" mechanism operated in the WGS reaction over Pt/Ce_{1-x}La_xO_{2-δ} catalysts ($x=0.0, 0.2$ and 1.0); M = Ce⁴⁺ or La³⁺.



Scheme 3. Reactive zone established around each Pt nanoparticle within which active —OH/H , HCOO— , and —COOH intermediate species found in the H-path and C-path of WGS reaction are formed. The extent (Δx , Å) of this reactive zone and the relative concentration of C-pool and H-pool within this zone depend on the $\text{Ce}_{1-x}\text{La}_x\text{O}_{2-\delta}$ support chemical composition ($x=0.0, 0.2$ and 1.0).

oxygen at the Pt–support interface, and the rate of their replenishment via water dissociation. It should be noted also that water dissociation is also possible on M–O sites of the metal oxide support [51,52]. Grabow et al. [42] reported that on Pt(111) surface formate formation via the single $\text{CO} + \text{OH}$ elementary step is prohibited on the basis of simple geometric considerations and binding modes of adsorbed CO and OH. On the other hand, based on in situ DRIFTS studies (not reported here), the concentration of formate (e.g., Figs. 5 and 7a) was significantly larger under 3%CO/10% H_2O /Ar than 3%CO/Ar or 985 ppm CO_2 /Ar gas treatments; it is noted that the concentration of 985 ppm CO_2 used was the same as that measured under 3%CO/10% H_2O /Ar reaction conditions. Based on these findings, it might be possible that formate formation by the participation of CO and OH groups on the $\text{Ce}_x\text{La}_{1-x}\text{O}_{2-\delta}$ support (Scheme 2) is less energetic demanding than on Pt alone.

A mechanism similar to that depicted in Scheme 2 could be proposed for the carboxyl (—COOH) intermediate.

3.7.1. Active WGS reaction zone (Δx , Å)

Based on the quantitative results reported in Tables 4 and 5 regarding the concentrations of active H-pool and C-pool intermediates, which are significantly larger than one monolayer of surface Pt_s ($\theta=1$), it is possible to estimate the extent (Δx , Å) of a reactive zone around each Pt nanoparticle which accommodates the majority of these intermediates, as depicted in Scheme 3. In this estimation, it is considered that after water dissociation, 1 surface lattice oxygen and 1 adjacent metal cation accommodate, respectively, 1 H and 1 OH species. Also, the stoichiometry of formate/carboxyl bonding with Pt and support sites, and that of adsorbed CO is 1:1 (see Scheme 2, Fig. 4). After estimating the number of Pt nanoparticles per gram of catalyst (no. $\text{Pt}_{\text{gcat}}^{-1}$), the site density of oxygen anions and metal cations on the support surface using crystallographic data (atoms nm^{-2}), the size of the hemispherical Pt nanoclusters (Table 1), and the concentration of active intermediates (mol/g , Tables 4 and 5), the length (Δx , Å) of a reactive zone around each Pt nanoparticle was found to be 2.6, 2.2, and 3.5 Å, respectively, for the $\text{Pt/La}_2\text{O}_3$, Pt/CeO_2 and $\text{Pt/Ce}_{0.8}\text{La}_{0.2}\text{O}_{2-\delta}$ catalytic systems (steady-state WGS reaction at 300 °C). The result of this analysis provides now good understanding on the relative specific kinetic rates reported in Table 3, where $\text{Pt/Ce}_{0.8}\text{La}_{0.2}\text{O}_{2-\delta}$ was found to be the most active catalytic system, whereas $\text{Pt/La}_2\text{O}_3$ the least active. These specific kinetic rates can now be linked with

the concentration of active intermediates around each Pt nanoparticle and the reactivity (k) of these sites.

Based on the length (Δx , Å) of the reactive zone reported above, it is clear that for all three catalytic systems this is equivalent to about one lattice constant (on the average) from the Pt–support interface. This important conclusion supports the suggested mode of bonding of formate (or carboxyl) at the metal–support interface and the kinetic rate analysis provided in Table 3 (rate expressed in terms of the length of the perimeter of Pt–support interface). Based on the results of Table 3, La_2O_3 specific activity expressed either as $\mu\text{mol g}^{-1} \text{s}^{-1}$ or $\mu\text{mol cm}^{-1} \text{s}^{-1}$ is lower by a factor of 2.8 compared to that of Pt supported on $\text{Ce}_{0.8}\text{La}_{0.2}\text{O}_{2-\delta}$. This can only be explained after considering that the site reactivity (k) for the WGS of $\text{Pt/Ce}_{0.8}\text{La}_{0.2}\text{O}_{2-\delta}$ is significantly larger than that of $\text{Pt/La}_2\text{O}_3$.

Given the fact that all three catalytic systems follow the “redox” mechanism for the WGS reaction at 300 °C, as previously discussed, it is suggested that (a) the presence of a significantly larger concentration ($\mu\text{mol O g}^{-1}$) of labile oxygen (OSC, not reported here) and oxygen vacancies in $\text{Ce}_{0.8}\text{La}_{0.2}\text{O}_{2-\delta}$ [15,26,73], and (b) the lower activation energy for reduction of $\text{Ce}_{0.8}\text{La}_{0.2}\text{O}_{2-\delta}$ compared to ceria and lanthana (H_2 -TPR studies not reported here) largely contribute to the enhanced magnitude of kinetic parameters (surface coverage and site reactivity) that cause the appearance of the promoting effect of La^{3+} -doping of ceria toward WGS activity.

There is a significant increase in the concentration of H-pool with reaction temperature from 250 to 300 °C in the case of $\text{Pt/Ce}_{0.8}\text{La}_{0.2}\text{O}_{2-\delta}$ (Table 4). This result could be explained by considering that water chemisorption and dissociation are important elementary steps on the surface of support. Surface diffusion of derived OH/H species toward appropriate sites within the “reactive zone” (Scheme 3) for the formation of $\text{H}_2(\text{g})$ is an activated process, and considering also the heterogeneous diffusion model reported by Martin and Duprez [74] for preferential diffusion paths, then the increase of reaction T is reasonably expected to increase the rate of diffusion and the participation of an increased concentration of such species to the formation of $\text{H}_2(\text{g})$. The steady-state surface concentration of these species at a given reaction T is controlled by the rates of their formation and consumption. The increase in the amount of active C-pool with reaction temperature was also observed (Table 5) but this increase remains smaller than that observed for the H-pool. The steady-state surface concentration of an active reaction intermediate is established based on the individual rates (formation and consumption) associated with that species. Since the increase in the surface concentration of active molecularly adsorbed CO with reaction temperature is not reasonable to be expected, the relative increase of surface CO diffusion rate from Pt to the support and within the reactive zone (Scheme 3) in forming active formate and carboxyl species with respect to the consumption rates of these species toward CO_2 and H_2 formation is a reasonable explanation for the 35% increase of C-pool from 250 to 300 °C (Table 5).

The important results and conclusions derived from the present mechanistic work on the WGS reaction on $\text{Pt/Ce}_{1-x}\text{La}_x\text{O}_{2-\delta}$ were obtained with a gas composition not consistent with that found in the outlet of a typical hydrocarbon-reformer (e.g., 10 vol% CO, 7 vol% CO_2 , 25 vol% H_2 , 25 vol% H_2O). The presence of large concentrations of CO_2 and H_2O would certainly promote the reverse WGS reaction, which in turn would affect the surface concentrations of active intermediates present in the forward WGS reaction. For example, formate intermediate can be formed via the reaction of CO_2 and H_2 on ceria and Pt surfaces [42,75]. The increase in the surface concentration of less reactive intermediates could lead to the blocking of surface catalytic sites, which in turn may change the rate-determining step. The formation of carbonates might be also expected to increase with increasing CO_2 feed concentration, and as a result of this blocking of active sites on the support is also possible,

which would also influence the shift in the rate-limiting step. On the other hand, it is difficult to predict if the relative contribution of “redox” versus “associative” mechanism would drastically change under the composition obtained from the outlet of a reformer compared to that used in the present work for investigating the WGS reaction. Similar transient isotopic work to the one reported here could be proved very beneficial in providing an answer to this important point.

4. Conclusions

The following conclusions can be considered based on the results of the present work:

The enhanced WGS catalytic activity ($\mu\text{mol g}^{-1} \text{s}^{-1}$ or $\mu\text{mol cm}^{-1} \text{s}^{-1}$) exhibited by $\text{Pt/Ce}_{0.8}\text{La}_{0.2}\text{O}_{2-\delta}$ compared to Pt/CeO_2 and $\text{Pt/La}_2\text{O}_3$ catalysts is explained by the higher site reactivity (k) of active “H-containing” and/or “C-containing” intermediates which were also formed in a larger surface concentration (mols nm^{-2}) within a reactive zone around each Pt nanoparticle ($d_{\text{Pt}} = 1.0\text{--}1.2 \text{ nm}$) characterized by a length of about one lattice constant.

The mechanism of WGS reaction over Pt (1.0–1.2 nm) supported on $\text{Ce}_{1-x}\text{La}_x\text{O}_{2-\delta}$ ($x = 0.0, 0.2$ and 1.0) in the 250–300 °C range using 10 vol% H_2O and a $\text{H}_2\text{O}/\text{CO}$ ratio of about 3.3 was found to proceed through the “redox” bifunctional mechanism and a parallel “associative with –OH group regeneration” mechanism via formate and carboxyl intermediates. The extent of participation of each reaction path to the overall kinetic rate of WGS in the 250–300 °C range was found to depend on the composition of support according to the present results and others reported earlier [16,17].

Three kinds of linear adsorbed CO associated with Pt and Pt–support sites are considered as active intermediates present in the carbon-path of WGS in the 250–300 °C range over Pt supported on $\text{Ce}_{0.8}\text{La}_{0.2}\text{O}_{2-\delta}$, among which the LF-linear CO was the most reactive toward water. In the case of Pt supported on CeO_2 , only two kinds of linear adsorbed CO were found [16].

Acknowledgements

The European Regional Development Fund, the Republic of Cyprus, and the Research Promotion Foundation of Cyprus are gratefully acknowledged for their financial support through the project TEXNO/0308(BE)/05.

References

- [1] W. McDowall, M. Eames, *Energy Policy* 34 (2006) 1236–1250.
- [2] F. Mueller-Langer, E. Tzimas, M. Kaltschmitt, S. Peteves, *International Journal of Hydrogen Energy* 32 (2007) 3797–3810.
- [3] S.R.A. European Hydrogen and Fuel Cell Technology Platform, *Strategic Research Agenda* 2005.
- [4] E.D. Park, D. Lee, H.C. Lee, *Catalysis Today* 139 (2009) 280–290.
- [5] A.C. Basagiannis, X.E. Verykios, *Applied Catalysis A: General* 308 (2006) 182–193.
- [6] S. Chernik, R. French, C. Feik, E. Chornet, *Industrial and Engineering Chemistry Research* 41 (2002) 4209–4215.
- [7] R.D. Cortright, R.R. Davda, J.A. Dumesic, *Nature* 418 (2002) 964–967.
- [8] Q. Fu, H. Saltsburg, M. Flytzani-Stephanopoulos, *Science* 301 (2003) 935–938.
- [9] D.S. Newsome, *Catalysis Reviews, Science and Engineering* 21 (1980) 275–318.
- [10] G. Jacobs, B.H. Davis, *Catalysis* 20 (2007) 122–285.
- [11] X.S. Liu, W. Ruettinger, X.M. Xu, R. Farrauto, *Applied Catalysis B: Environmental* 56 (2005) 69–75.
- [12] X. Wang, R.J. Gorte, J.P. Wagner, *Journal of Catalysis* 212 (2002) 225–230.
- [13] K.G. Azzam, I.V. Babich, K. Seshan, L. Lefferts, *Journal of Catalysis* 251 (2007) 153–162.
- [14] K.G. Azzam, I.V. Babich, K. Seshan, L. Lefferts, *Journal of Catalysis* 251 (2007) 163–171.
- [15] S. Ricote, G. Jacobs, M. Milling, Y. Ji, P.M. Patterson, B.H. Davis, *Applied Catalysis A: General* 303 (2006) 35–47.
- [16] C.M. Kalamaras, S. Americanou, A.M. Efstathiou, *Journal of Catalysis* 279 (2011) 287–300.
- [17] C.M. Kalamaras, D. Dionysiou, A.M. Efstathiou, *ACS Catalysis* 2 (2012) 2729–2742.
- [18] C.M. Kalamaras, I.D. Gonzalez, R.M. Navarro, J.L.G. Fierro, A.M. Efstathiou, *Journal of Physical Chemistry C* 115 (2011) 11595–11610.
- [19] C.M. Kalamaras, P. Panagiotopoulou, D.I. Kondarides, A.M. Efstathiou, *Journal of Catalysis* 264 (2009) 117–129.
- [20] V. Idakiev, T. Tabakova, K. Tenchev, Z.-Y. Yuan, T.-Z. Ren, B.-L. Su, *Catalysis Today* 128 (2007) 223–229.
- [21] K.G. Azzam, I.V. Babich, K. Seshan, L. Lefferts, *Applied Catalysis B: Environmental* 80 (2008) 129.
- [22] P. Panagiotopoulou, D.I. Kondarides, *Catalysis Today* 127 (2007) 319–329.
- [23] Y. Wang, S. Liang, A. Cao, R.L. Thompson, G. Veser, *Applied Catalysis B: Environmental* 99 (2010) 89–95.
- [24] A.M. Duarte de Farias, D. Nguyen-Thanh, M.A. Fraga, *Applied Catalysis B: Environmental* 93 (2010) 250–258.
- [25] H.C. Lee, D. Lee, O.Y. Lim, S. Kim, Y.T. Kim, E.Y. Ko, *Studies in Surface Science and Catalysis* 167 (2007) 201–206.
- [26] C.I. Vignatti, M.S. Avila, C.R. Apesteguia, T.F. Garetto, *Catalysis Today* 171 (2011) 297–303.
- [27] R. Burch, *Physical Chemistry Chemical Physics* 8 (2006) 5483–5500.
- [28] F.C. Meunier, *Catalysis Today* 155 (2010) 164–171.
- [29] A.M. Efstathiou, J.T. Gleaves, G.S. Yablonsky, *Characterization of Solid Materials and Heterogeneous Catalysts: From Structure to Surface Reactivity*, Wiley-VCH, 2012, pp. 1013–1073 (Chapter 22).
- [30] T. Bunluesin, R.J. Gorte, G.W. Graham, *Applied Catalysis B: Environmental* 15 (1998) 107–114.
- [31] R.J. Gorte, S. Zhao, *Catalysis Today* 104 (2005) 18–24.
- [32] S. Hilaire, X. Wang, T. Luo, R.J. Gorte, J. Wagner, *Applied Catalysis A: General* 215 (2001) 271–278.
- [33] Y. Li, Q. Fu, M. Flytzani-Stephanopoulos, *Applied Catalysis B: Environmental* 27 (2000) 179–191.
- [34] W. Liu, M. Flytzani-Stephanopoulos, *Journal of Catalysis* 153 (1995) 317–332.
- [35] B.A.A. Silberova, M.M.G. Mul, J.A. Moulijn, *Journal of Catalysis* 243 (2006) 171–182.
- [36] E. Chenu, G. Jacobs, A.C. Crawford, R.A. Keogh, P.M. Patterson, D.E. Sparks, B.H. Davis, *Applied Catalysis B: Environmental* 59 (2005) 45–58.
- [37] G. Jacobs, U.M. Graham, E. Chenu, P.M. Patterson, A. Dozier, B.H. Davis, *Journal of Catalysis* 229 (2005) 499–512.
- [38] G. Jacobs, L. Williams, U. Graham, D. Sparks, B.H. Davis, *Journal of Physical Chemistry B* 107 (2003) 10398–10404.
- [39] G. Jacobs, L. Williams, U. Graham, G.A. Thomas, D.E. Sparks, B.H. Davis, *Applied Catalysis A: General* 252 (2003) 107–118.
- [40] T. Shido, Y. Iwasawa, *Journal of Catalysis* 141 (1993) 71–81.
- [41] A.A. Gokhale, J.A. Dumesic, M. Mavrikakis, *Journal of the American Chemical Society* 130 (2008) 1402–1414.
- [42] L.C. Grabow, A.A. Gokhale, S.T. Evans, J.A. Dumesic, M. Mavrikakis, *Journal of Physical Chemistry C* 112 (2008) 4608–4617.
- [43] D. Duprez, *Catalysis Today* 112 (2006) 17–22.
- [44] G. Jacobs, A.C. Crawford, B.H. Davis, *Catalysis Letters* 100 (2005) 147–152.
- [45] F.C. Meunier, A. Goguet, C. Hardacre, R. Burch, D. Thompson, *Journal of Catalysis* 252 (2007) 18–22.
- [46] F.C. Meunier, D. Reid, A. Goguet, S. Shekhtman, C. Hardacre, R. Burch, W. Deng, M.F. Stephanopoulos, *Journal of Catalysis* 247 (2007) 277–287.
- [47] M. Stamatakis, Y. Chen, D.G. Vlachos, *Journal of Physical Chemistry C* 115 (2011) 24750–24762.
- [48] D. Dionysiou, X. Qi, Y.S. Lin, G. Meng, D. Peng, *Journal of Membrane Science* 154 (1999) 143–153.
- [49] K. Polychronopoulou, C.N. Costa, A.M. Efstathiou, *Applied Catalysis A: General* 272 (2004) 37–52.
- [50] A.M. Efstathiou, X.E. Verykios, *Applied Catalysis A: General* 151 (1997) 109–166.
- [51] C.M. Kalamaras, G.G. Olympiou, A.M. Efstathiou, *Catalysis Today* 138 (2008) 228–234.
- [52] G.G. Olympiou, C.M. Kalamaras, C.D. Zeinalipour-Yazdi, A.M. Efstathiou, *Catalysis Today* 127 (2007) 304–318.
- [53] J. Sirta, S. Phanichphant, F.C. Meunier, *Analytical Chemistry* 79 (2007) 3912–3918.
- [54] D.A. Constantinou, M.C. Álvarez-Galván, J.L.G. Fierro, A.M. Efstathiou, *Applied Catalysis B: Environmental* 117–118 (2012) 81–95.
- [55] S. Bernal, M.A. Cauqui, G.A. Cifredo, J.M. Gatica, C. Larese, J.A. Pérez Omil, *Catalysis Today* 29 (1996) 77–81.
- [56] G. Jacobs, B.H. Davis, *Applied Catalysis A: General* 333 (2007) 192–201.
- [57] M. Menetrey, A. Markovits, C. Minot, *Surface Science* 524 (2003) 49–62.
- [58] R. Leppelt, B. Schumacher, V. Plzak, M. Kinne, R.J. Behm, *Journal of Catalysis* 244 (2006) 137–152.
- [59] G. Balducci, J. Kaspar, P. Fornasiero, M. Graziani, M.S. Islam, *Journal of Physical Chemistry B* 102 (1998) 557–561.
- [60] S.L. Shannon, J.G. Goodwin Jr., *Chemical Reviews* 95 (1995) 677–695.
- [61] C. Li, Y. Sakata, T. Arai, K. Domen, K.-i. Maruya, T. Onishi, *Journal of the Chemical Society, Faraday Transactions I* 85 (1989) 929–943.
- [62] P. Bazin, O. Saur, J.C. Lavalley, M. Daturi, G. Blanchard, *Physical Chemistry Chemical Physics* 7 (2005) 187–194.
- [63] M. Primet, *Journal of Catalysis* 88 (1984) 273–282.
- [64] D. Tibiletti, A. Goguet, D. Reid, F.C. Meunier, R. Burch, *Catalysis Today* 113 (2006) 94–101.
- [65] G. Jacobs, S. Ricote, B.H. Davis, *Applied Catalysis A: General* 302 (2006) 14–21.

- [66] T. Shido, Y. Iwasawa, *Journal of Catalysis* 136 (1992) 493–503.
- [67] C.D. Zeinalipour-Yazdi, A.M. Efstathiou, *Journal of Physical Chemistry C* 112 (2008) 19030–19039.
- [68] F.C. Meunier, D. Tibiletti, A. Goguet, S. Shekhtman, C. Hardacre, R. Burch, *Catalysis Today* 126 (2007) 143–147.
- [69] D.C. Grenoble, M.M. Estadt, D.F. Ollis, *Journal of Catalysis* 67 (1981) 90–102.
- [70] G. Jacobs, S. Khalid, P.M. Patterson, D.E. Sparks, B.H. Davis, *Applied Catalysis A: General* 268 (2004) 255–266.
- [71] G. Jacobs, P.M. Patterson, U.M. Graham, A.C. Crawford, B.H. Davis, *International Journal of Hydrogen Energy* 30 (2005) 1265–1276.
- [72] G. Jacobs, P.M. Patterson, L. Williams, E. Chenu, D. Sparks, G. Thomas, B.H. Davis, *Applied Catalysis A: General* 262 (2004) 177–187.
- [73] Y.T. Kim, S.J. You, E.D. Park, *International Journal of Hydrogen Energy* 37 (2012) 1465–1474.
- [74] D. Martin, D. Duprez, *Journal of Physical Chemistry B* 101 (1997) 4428–4436.
- [75] A. Goguet, F.C. Meunier, D. Tibiletti, J.P. Breen, R. Burch, *Journal of Physical Chemistry B* 108 (2004) 20240–20246.